

Defining the (Black Hole)-Spheroid Connection with the Discovery of Morphology-Dependent Substructure in the $M_{\text{BH}}-n_{\text{sph}}$ and $M_{\text{BH}}-R_{\text{e,sph}}$ Diagrams: New Tests for Advanced Theories and Realistic Simulations

NANDINI SAHU ^{1,2} ALISTER W. GRAHAM ² AND BENJAMIN L. DAVIS ²

¹*OzGrav-Swinburne, Centre for Astrophysics and Supercomputing, Swinburne University of Technology, Hawthorn, VIC 3122, Australia*
²*Centre for Astrophysics and Supercomputing, Swinburne University of Technology, Hawthorn, VIC 3122, Australia*

(Published 2020 November 06 in the *Astrophysical Journal*)

ABSTRACT

For 123 local galaxies with directly-measured black hole masses (M_{BH}), we provide the host spheroid’s Sérsic index (n_{sph}), effective half-light radius ($R_{\text{e,sph}}$), and effective surface brightness (μ_e), obtained from careful multi-component decompositions, and we use these to derive the morphology-dependent $M_{\text{BH}}-n_{\text{sph}}$ and $M_{\text{BH}}-R_{\text{e,sph}}$ relations. We additionally present the morphology-dependent $M_{\text{BH}}-M_{*,\text{sph}}$ and $M_{*,\text{sph}}-R_{\text{e,sph}}$ relations. We explored differences due to: early-type galaxies (ETGs) versus late-type galaxies (LTGs); Sérsic versus core-Sérsic galaxies; barred versus non-barred galaxies; and galaxies with and without a stellar disk. We detect two different $M_{\text{BH}}-n_{\text{sph}}$ relations due to ETGs and LTGs with power-law slopes 3.95 ± 0.34 and 2.85 ± 0.31 . We additionally quantified the correlation between M_{BH} and the spheroid’s central concentration index, which varies monotonically with the Sérsic index. Furthermore, we observe a single, near-linear $M_{*,\text{sph}}-R_{\text{e,sph}}^{1.08 \pm 0.04}$ relation for ETGs and LTGs, which encompasses both classical and alleged pseudobulges. In contrast, ETGs and LTGs define two distinct $M_{\text{BH}}-R_{\text{e,sph}}$ relations with $\Delta_{\text{rms}|_{\text{BH}}} \sim 0.60$ dex (cf. ~ 0.51 dex for the $M_{\text{BH}}-\sigma$ relation and ~ 0.58 dex for the $M_{\text{BH}}-M_{*,\text{sph}}$ relation), and the ETGs alone define two steeper $M_{\text{BH}}-R_{\text{e,sph}}$ relations, offset by ~ 1 dex in the $\log M_{\text{BH}}$ -direction, depending on whether they have a disk or not and explaining their similar offset in the $M_{\text{BH}}-M_{*,\text{sph}}$ diagram. This trend holds using 10%, 50%, or 90% radii. These relations offer pivotal checks for simulations trying to reproduce realistic galaxies, and for theoretical studies investigating the dependency of black hole mass on basic spheroid properties.

Keywords: black hole physics — galaxies: evolution — galaxies: elliptical and lenticular, cD — galaxies: spiral — galaxies: structure

1. INTRODUCTION

It is widely known that the mass of the black hole (BH) residing at the centre of most galaxies is correlated with both the host spheroid’s stellar mass ($M_{*,\text{sph}}$) and its central stellar velocity dispersion (σ). At the same time, bulgeless galaxies, for example, NGC 2478, NGC 4395, and NGC 6926, have also been observed to house massive BHs (e.g. [Secrest et al. 2013](#); [Simmons et al. 2013](#); [den Brok et al. 2015](#); [Davis et al. 2019](#),

and references therein), and one of the tightest scaling relations is between black hole mass (M_{BH}) and the winding/pitch angle of the spiral arms in spiral galaxies ([Seigar et al. 2008](#); [Berrier et al. 2013](#); [Davis et al. 2017](#)). Additional correlations exist between M_{BH} and disk stellar mass ([Davis et al. 2018](#)), disk rotation, and dark matter halo mass ([Ferrarese 2002](#); [Baes et al. 2003](#); [Volonteri et al. 2011](#); [Davis et al. 2019](#)). Collectively, this goes beyond the notion of a single primary (causal) relation for all galaxies plus secondary (indirect/consequential) relations, and reveals a greater level of complexity. Indeed, the markedly different $M_{\text{BH}}-M_{*,\text{gal}}$ and $M_{\text{BH}}-M_{*,\text{sph}}$ relations for early-type galaxies (ETGs, comprised of E-

ES¹-, and S0-types) and late-type galaxies (LTGs), i.e. spiral (Sp) galaxies (Davis et al. 2018; Davis et al. 2019; Sahu et al. 2019a), undoubtedly reflects the different physical processes, gas supply history, net angular momentum, involved in building these systems.

The review of the BH scaling relations by Graham (2016) highlighted the need to achieve internal consistency among the various scaling relations, in particular between the $M_{\text{BH}}-\sigma$, $M_{\text{BH}}-M_{*,\text{sph}}$, and $\sigma-M_{*,\text{sph}}$ relations. This followed Graham (2012) who reported on a near-linear and super-quadratic $M_{\text{BH}}-M_{*,\text{sph}}$ relation, respectively, for spheroids with a Sérsic or core-Sérsic² light profile (see also Graham & Scott (2013) and Scott et al. (2013)). Savorgnan et al. (2016) subsequently discovered an improved division due to ETGs and LTGs (none of LTGs have core-Sérsic bulge profiles) in the $M_{\text{BH}}-M_{*,\text{sph}}$ diagram, and in the $M_{\text{BH}}-(L_{\text{gal}}, \text{galaxy luminosity})$ diagram. This was also later reported by van den Bosch (2016). Savorgnan et al. (2016) coined the notion of a red and blue sequence when two tracks, due to ETGs and LTGs, are evident in a BH mass scaling diagram (see also Terrazas et al. 2016; Dullo et al. 2020). Sahu et al. (2019a) additionally found that the $M_{\text{BH}}-M_{*,\text{sph}}$ relation for ETGs with a disk (ES and S0) and ETGs without a disk (E-type) is roughly quadratic, while the two relations are offset by more than an order of magnitude in the M_{BH} -direction. This has since been found in a recent simulation by Marshall et al. (2020). Clearly, it is not simply the amount of stellar mass that matters, but also how it was accumulated and is now distributed. In this vein, we explore the relationship that the BH mass has with the size and shape (centrally concentrated or diffused) of the surrounding bulge/spheroid— terms that we use interchangeably— and as a function of the morphology of the host galaxy.

The above mentioned developments represent a key advance in our understanding of the coevolution of galaxies and black holes. It built upon works such as Wandel (1999), Salucci et al. (2000), Laor (2001), and Graham (2012) and voided the notion (Dressler 1989; Kormendy & Richstone 1995; Magorrian et al. 1998) that the black hole mass simply co-evolved linearly with the spheroid mass. The recognition of a more nuanced situation is perhaps not surprising given the va-

riety of accretion/merger histories, and resulting structures among galaxies. For example, core-Sérsic galaxies, thought to be built from the dry merger of galaxies with pre-existing black holes (Begelman 1984), appear to follow a steeper relation in the $M_{\text{BH}}-\sigma$ diagram (Sahu et al. 2019b), see also Terrazas et al. (2016, their Figure 3a) and Bogdán et al. (2018, their Figure 5).

Based on the low intrinsic scatter about the $M_{\text{BH}}-\sigma$ relation (Ferrarese & Merritt 2000; Gebhardt et al. 2000), some studies have concluded that it is the most fundamental relation between black hole mass and galaxy (e.g. van den Bosch 2016; de Nicola et al. 2019). However, it may be a premature conclusion without considering the correlations between BH mass and other basic galaxy properties, or allowing for the morphology-dependence and thus (formation physics)-dependence of galaxies. Moreover, it overlooks that the $M_{\text{BH}}-\text{pitch angle } (\phi)$ relation has the least total scatter at 0.43 dex (Davis et al. 2017) compared to 0.51 dex in the latest $M_{\text{BH}}-\sigma$ diagram (Sahu et al. 2019b).

Establishing if a, and which, single relation is the most fundamental, i.e., the primary relation, and how it depends upon morphology is important for understanding the co-evolution of galaxies and BHs. The secondary scaling relations — not to be confused with the morphology dependent substructure which reveals an additional parameter/factor modulating the co-joined growth of galaxies and BHs³ — are, however, also important. They can still be used, for example, to predict BH masses or to check on the accuracy of computer simulations e.g., CLUES (Yepes et al. 2009), Magenticum (Dolag 2015), Bolshoi (Klypin et al. 2011), EAGLE (Schaye et al. 2015), Illustris (Vogelsberger et al. 2014), IllustrisTNG (Pillepich et al. 2018), FIRE (Hopkins et al. 2018), and SIMBA (Davé et al. 2019), which are trying to produce realistic galaxies⁴. These empirical relations help to decipher the physics behind the effect of the central supermassive black hole on the host spheroid/galaxy properties and vice versa. How such black hole feedback drives galaxy evolution is the challenge yet to be fully answered (Choi et al. 2018;

¹ ES-type represents elliptical galaxies which have an intermediate-scale stellar disk confined to within their spheroid (Liller 1966; Graham 2019a).

² Core-Sérsic galaxies have a deficit of light at their centre; hence, their central (bulge) light profile is described using a shallow power-law followed by a Sérsic (1963) function beyond the core (Graham et al. 2003b). This population was first discussed by King & Minkowski (1966, 1972).

³ We could re-frame these results by constructing a simplified ‘fundamental plane’, i.e. a 3-parameter equation involving M_{BH} , σ (or M_*) and morphological type (even if just a binary parameter). This would effectively unite the morphology-dependent $M_{\text{BH}}-\sigma$ ($M_{\text{BH}}-M_*$) relations and reduce the scatter about the two-parameter relations which ignore the morphological type. We will pursue this in future work.

⁴ Simulations lacking primary information about the spheroid can still be tested against the non-linear, morphology-dependent, $M_{\text{BH}}-M_{*,\text{gal}}$ relations (Davis et al. 2018; Sahu et al. 2019a).

Ruszkowski et al. 2019; Terrazas et al. 2020; Martín-Navarro et al. 2020).

Here, we will expand upon the previous efforts in establishing the $M_{\text{BH}}-n_{\text{sph}}$ relation (e.g., Graham et al. 2003a; Graham & Driver 2007a; Vika et al. 2012; Beifiori et al. 2012; Savorgnan et al. 2013; Savorgnan 2016), the $M_{*,\text{sph}}-n_{\text{sph}}$ relation (e.g., Andredakis et al. 1995; Jerjen et al. 2000; Graham & Guzmán 2003; Ferrarese et al. 2006; Savorgnan 2016), the $M_{*,\text{sph}}-R_{\text{e,sph}}$ relation (e.g., Sérsic 1968a; Graham & Worley 2008; Lange et al. 2015), and the $M_{\text{BH}}-R_{\text{e,sph}}$ relation (e.g., de Nicola et al. 2019) using our extensive sample of 83 ETGs and 40 LTGs with careful (individual, not automated) multi-component decompositions. Importantly, we explore potential substructures due to galaxy sub-morphologies, i.e., Sérsic versus core-Sérsic galaxies, barred versus non-barred galaxies, galaxies with a stellar disk versus galaxies without a stellar disk, and ETGs versus LTGs. We also investigate the relation between M_{BH} and the central concentration index (Graham et al. 2001a), which is known to vary monotonically with the Sérsic index (Trujillo et al. 2001; Graham et al. 2001b).

As with the $M_{\text{BH}}-M_{*,\text{sph}}$ relation, the $M_{\text{BH}}-n_{\text{sph}}$ and $M_{\text{BH}}-R_{\text{e,sph}}$ relations can be applied to large surveys of galaxies (e.g., Casura et al. 2019) — if their bulge Sérsic parameters are reliable — to estimate their black hole masses and further construct the black hole mass function (BHMF). The BHMF holds interesting information for cosmologists, e.g., to estimate the mass density of the Universe contained in BHs (e.g. Fukugita & Peebles 2004; Graham & Driver 2007b), to map the growth of BHs and constrain theoretical models of BH evolution (e.g. Kelly & Merloni 2012). In addition, the latest BHMF, which takes part in calculating the black hole merger rate (Chen et al. 2019; Volonteri et al. 2020), will help improve the prediction for the amplitude and time until detection of the long-wavelength (micro to nano Hertz) gravitation wave background — as generated from merging supermassive black holes — using pulsar timing arrays (Siemens et al. 2013; Shannon et al. 2015; Sesana et al. 2016) and using the upcoming Laser Interferometer Space Antenna (LISA, Danzmann 2017; Baker et al. 2019).

Section 2 details the galaxy sample and parameters which we used for our investigation, and the regression routines applied to obtain the correlations. Various correlations we observed, including their dependencies on galaxy morphology, are described in the subsections of Section 3. In sub-section 3.1, we present the scaling relations observed between the spheroid stellar mass and spheroid Sérsic index. Sub-section 3.2 presents the expected correlation between black hole mass and the

bulge Sérsic index by combing the correlation observed between spheroid stellar mass and spheroid Sérsic index with our latest correlation between black hole mass and spheroid stellar mass. It then presents the observed correlations between black hole mass and the bulge Sérsic index based on our data-set. We also show the relationship between the Sérsic index and the central light concentration, and we present the correlation observed between the black hole mass and the central concentration index. In sub-section 3.3, we present the correlations observed between the spheroid stellar mass and the effective spheroid half-light radius. Here, we also explore the correlations of the spheroid stellar mass with the spheroid radii containing 10% and 90% of the light of the spheroid. Sub-section 3.4 provides the expected correlation that the spheroid half-light radius might have with the black hole mass, before presenting the observed correlations between the black hole mass and the spheroid effective half-light radius, along with the correlations between the black hole mass and the spheroid radii containing 10% and 90% of spheroid’s light. These subsections additionally provide a discussion and some explanation for the correlations that we find. Finally, Section 4 presents a summary of our main results.

2. DATA

The Sérsic (1963, 1968a) function is nowadays used to describe the light profiles of elliptical galaxies (E) and, when present, the spheroidal component of galaxies with a disk (ES/S0/Sp). A review of the Sérsic function, and its many associated expressions, can be found in Graham & Driver (2005). Briefly, the intensity of a Sérsic light profile can be expressed as a function of the projected galactic radius (R), such that

$$I(R) = I_e \exp \left[-b_n \left\{ \left(\frac{R}{R_e} \right)^{1/n} - 1 \right\} \right], \quad (1)$$

where I_e , R_e , and n are profile parameters. The term I_e is the effective intensity at the effective radius R_e , which bounds 50% of the total light in the associated 2D image. Graham (2019b) provides a detailed review of this popular radius and addresses the misconceptions about its physical significance. The surface brightness at this effective radius (μ_e) is related to I_e through $\mu_e \equiv -2.5 \log(I_e)$.

The Sérsic index n (also known as the shape parameter), describes the curvature of the light profile, such that a Sérsic light profile with a higher Sérsic index is steeper at the centre and has a shallower distribution at larger radius, whereas, a profile with a smaller Sérsic index is shallower at the centre followed by a steeper drop at outer radii (see Figure 2 in Graham 2019b). Thus,

the Sérsic index traces the central concentration of the light within the spheroid (Trujillo et al. 2001; Graham et al. 2001b, their Figure 2); and also the inner gradient of the gravitational potential⁵ (Terzić & Graham 2005, their Figures 2 and 3). The value of the term b_n in Equation 1 depends on n , and is obtained by solving $\Gamma(2n) = 2\gamma(2n, b_n)$, where Γ denotes the gamma function and γ is the incomplete gamma function. It can also be approximated by $b_n \approx 1.9992n - 0.3271$ for $0.5 < n < 10$ (Capaccioli 1989).

In this work, we have used a sample of 123 galaxies with directly-measured black hole masses, for whom the Sérsic model parameters (n, R_e , and μ_e) describing their spheroid’s surface brightness distribution were obtained by a careful multi-component decomposition of the galaxy’s light. These parameters are collectively taken from Savorgnan & Graham (2016), Davis et al. (2019), and Sahu et al. (2019a). These studies performed a 2-dimensional (2D) isophotal analysis, first extracting a 2D luminosity model using ISOFIT and CMODEL (Ciambur 2015) to capture the radial gradients in the ellipticity, position angle, and Fourier harmonic coefficients describing the isophote’s deviations from a pure ellipse, and then performing a multi-component decomposition using the isophotal-averaged 1D surface-brightness profile along the major and geometric-mean⁶ axis of the galaxies. For this purpose, they used the software PROFILER (Ciambur 2016), which is inbuilt with many functions for specific galaxy components, including the Sérsic function for galactic spheroids. The major and geometric-mean axis were modelled independently (see Section 3 in Sahu et al. 2019a, for more details).

Table A1 in our appendix lists both the major-axis bulge parameters ($n_{\text{maj}}, R_{e,\text{maj}}, \mu_{e,\text{maj}}$), and the equivalent-axis bulge parameters ($n_{\text{eq}}, R_{e,\text{eq}}, \mu_{e,\text{eq}}$), plus the morphologies, and the bulge masses ($M_{*,\text{sph}}$) taken from Savorgnan & Graham (2016), Davis et al. (2019), and Sahu et al. (2019a), along with the distances and the directly-measured black hole masses of the galaxies. To show the consistency between the structural decomposition of the major- and equivalent-axis surface brightness profiles, we have plotted $\mu_{e,\text{sph,maj}}$ versus

$\mu_{e,\text{sph,eq}}$ in Figure 1. The 1σ scatter in this diagram is $0.58 \text{ mag arcsec}^{-2}$ which corresponds to a 1σ scatter in R_e of $\approx 30\%$ given that the Sérsic model’s surface brightness profile has slopes of ~ 1.8 to ~ 2.1 (for $n = 1$ to 10) at $R = R_e$, where $d\mu(R)/dR|_{R_e} = 2.5b_n/(\ln(10)nR_e) \approx [2.17 - 0.36/n]/R_e$. Table A1 also provides the radial concentration index (C: see Section 3) and the physical (arcsec to kpc) size scale of the galaxies⁷. The morphologies of these galaxies are based on the multi-component decompositions found in Savorgnan & Graham (2016), Davis et al. (2019), and Sahu et al. (2019a).

The black hole masses used here have been obtained from various sources in the literature. Their original sources are listed in Savorgnan et al. (2016) and Sahu et al. (2019a) for the ETGs, and in Davis et al. (2019) for the LTGs. These black hole masses have been directly-measured using either the stellar dynamical modelling, gas dynamical modelling, megamaser kinematics, proper motions (Sgr A^*), or the latest direct imaging method (M87*). As the distances to the galaxies have been revised over time, the BH masses have also been updated to keep pace with this, and thereby provide a consistent analysis with the arcsecond-to-kpc and apparent-to-absolute magnitude conversions.

Our total sample is comprised of 123 galaxies, of which 83 are ETGs, and 40 are LTGs. We have used the Bivariate Correlated Errors and Intrinsic Scatter (BCES) regression (Akritas & Bershady 1996) to obtain the symmetric (bisector) best-fit lines for all our correlations. The BCES⁸ regression considers the measurement errors in both variables and allows for intrinsic scatter in the data. It is a modified form of the ordinary least square (OLS) regression. It calculates the OLS($Y|X$) line by minimizing the scatter in the Y-direction, and the OLS($X|Y$) line by minimizing the scatter in the X-direction. The BCES(BISECTOR) line symmetrically bisects the OLS($Y|X$) and OLS($X|Y$) lines. We prefer to use the bisector line as it offers equal treatment to the quantities plotted on the X- and Y-axes. Additionally, we also checked the consistency of our correlations by employing the modified-FITEXY (MPFITEXY) regression (Press et al. 1992; Tremaine et al. 2002; Williams et al. 2010; Markwardt 2012), where we had to bisect the best-fit lines ob-

⁵ This holds when dark matter is negligible, and there is no significant stellar mass-to-light ratio gradient.

⁶ The geometric-mean axis, which is also known as the “equivalent axis”, is the radius of the circularized form of the elliptical isophote with major axis radius R_{maj} and minor axis radius R_{min} , which conserves the same amount of flux. This results in the equivalent axis radius (R_{eq}) being the geometric mean of R_{maj} and R_{min} ($R_{\text{eq}} = \sqrt{R_{\text{maj}} * R_{\text{min}}}$), which is also represented as R_{geom} (for more details see the appendix section in Ciambur 2015).

⁷ The physical scale is calculated using the python version of Edward (Ned) L. Wright’s cosmological calculator (Wright 2006), written by James Schombert, assuming the cosmological parameters $H_0 = 67.4 \text{ (km s}^{-1}\text{)/Mpc}$, $\Omega_m = 0.315$, and $\Omega_v = 0.685$ (Planck Collaboration et al. 2018).

⁸ We used the Python module from (Nemmen et al. 2012), which is available at <https://github.com/rsnemmen/BCES>

tained from the forward MPFITEXY($Y|X$) and inverse MPFITEXY($X|Y$) regressions to obtain the symmetric fit to our data (see Novak et al. 2006, for more details about the MPFITEXY regression).

For our investigation, we adopt a 20% uncertainty for the Sérsic bulge parameter n . Various factors which can contribute to the uncertainty in the measurement of the Sérsic bulge parameters include: inappropriate sky subtraction; incomplete masking; inaccurate point-spread function (PSF) for the telescope; uncertainties in the identification of components; especially the nuclear (bar/disk/ring/star cluster) or faint components during the multi-component decomposition of the galaxy luminosity. Thus, it is challenging to quantify the uncertainty in the bulge parameters for every galaxy individually.

In past studies, various measures have been taken to quantify realistic errors on the bulge/galaxy Sérsic index. For example, Caon et al. (1993a) noted a typical error of $\sim 25\%$ corresponding to a 25% variation in the (observed - fitted) residual, while some studies (e.g. Graham & Driver 2007a; Savorgnan et al. 2013) adopted a constant uncertainty of $\sim 20\%$, and others employed Monte Carlo simulations (e.g. Beifiori et al. (2012) obtaining up to a $\sim 15\%$ error-bar). Others varied the sky subtraction by $\pm 1\sigma$ to estimate error-bars (Vika et al. 2012), some used mean/median errors based on a broader comparison with published parameters from other studies (Graham & Worley 2008; Laurikainen et al. 2010) producing up to $\sim 30\%$ uncertainty, whereas Savorgnan (2016) used 20%, 42%, and 52% uncertainties, respectively, for their grade 1, grade 2, and grade 3 galaxies following Savorgnan & Graham (2016, their Section 4.2). As Savorgnan & Graham (2016) noted, their generous uncertainties arose when comparing published parameters based upon an array of differing decompositions for the same galaxy. For example, sometimes a single Sérsic component had been fit while other times the image analysis additionally included, as separate components, a disk and sometimes also a bar.

Given that our sky-background intensities are measured carefully (Sahu et al. 2019a, see their Figure 1 and Section 2.2), and that our parameters are obtained from multi-component decompositions, we have ruled out our two major sources of systematic errors (i.e. over/under-estimation of the sky and failing to account for a biasing component), and as such we adopt a 20% uncertainty for n , and a 30% uncertainty for R_{e} based on the 1σ scatter in μ_{e} for our galaxy sample as already described in this section. We do, however, test and confirm that our scaling relations are not significantly dependent upon this. Our results are stable (no change in slope or intercept at

the 1σ uncertainty level) upon using an uncertainty up to 30% in n and 40% in R_{e} . Furthermore, we also performed all the correlations using the major subsample of our total sample for whom the spheroid parameters are derived using $3.6\mu\text{m}$ images (see Table A1), and the correlations are found to be consistent with the correlations obtained using the total sample within the $\pm 1\sigma$ uncertainty bounds of the slopes and intercepts.

During our linear regressions, we have excluded certain potentially biasing galaxies, which are either stripped galaxies (NGC 4342 and NGC 4486B), a single galaxy with $M_{\text{BH}} < 10^5 M_{\odot}$ (NGC 404), or more than 2σ outliers (NGC 1300, NGC 3377, NGC 3998, NGC 4945, NGC 5419) in any of the correlations presented here. NGC 4342 and NGC 4486B are stripped of their stellar mass due to the gravitational pull of their massive companion galaxies NGC 4365 (Blom et al. 2014) and NGC 4486 (Batcheldor et al. 2010), respectively. Hence, NGC 4342 and NGC 4486B can bias the black hole scaling relations as they have smaller n or R_{e} than they would have had if they weren't stripped of their mass. NGC 404, the only galaxy in our sample with a BH mass below $10^6 M_{\odot}$, can bias the best-fit lines due to its location at the end of the distribution and thus its elevated torque strength. The galaxies NGC 3377, NGC 3998, NGC 4945, and NGC 5419 in the $M_{\text{BH}}-n$ diagram, and NGC 1300 in the $M_{\text{BH}}-R_{\text{e}}$ diagram, are more than $\pm 2\sigma_{\text{rms}}$ outliers from the corresponding best-fit lines and slightly alter their slopes⁹. Hence, these galaxies are better excluded in all our regressions to obtain robust correlations. These eight excluded galaxies are indicated in all the plots. This exclusion leaves us with a reduced sample of 115 galaxies.

3. SCALING RELATIONS

The stellar masses of our galactic spheroids ($M_{*,\text{sph}}$) are derived from the luminosities measured using the Sérsic model (for the bulge) fit to the equivalent- (or geometric-mean) axis light profile, parameterized by $n_{\text{sph,eq}}$, $R_{\text{e,sph,eq}}$, and $I_{\text{e,sph,eq}}$. Therefore, it is expected to find some correlation between $M_{*,\text{sph}}$ and the Sérsic index, and also between $M_{*,\text{sph}}$ and the effective half-light radius. The issue of parameter coupling potentially explaining the trends between the Sérsic parameters and the luminosity was explored and dismissed using model-independent measures of both luminosity and size (Caon et al. 1993b; Trujillo et al. 2001), implying the observed correlation between luminosity versus Sérsic properties (n and R_{e}) are indeed real. Moreover, the errors in n

⁹ Including these galaxies in the regressions changes the slopes by $\sim 1\sigma$ uncertainty level of current slopes.

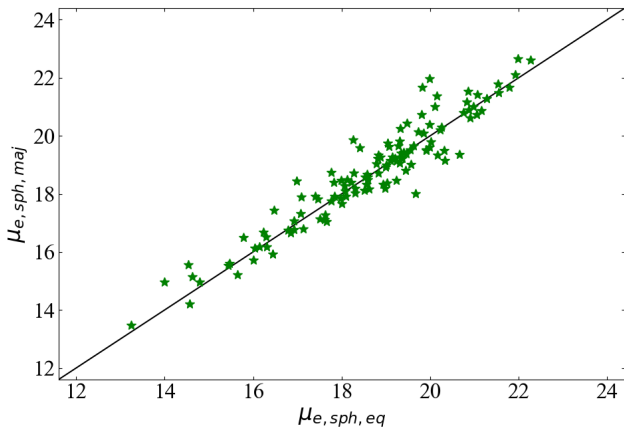


Figure 1. The spheroid surface brightness at the effective half-light radius from a Sérsic fit to the major-axis light profile ($\mu_{e,\text{sph,maj}}$) plotted against the spheroid surface brightness at the effective half-light radius from a Sérsic fit to the the geometric mean-axis light profile ($\mu_{e,\text{sph,eq}}$). This tight distribution of data-points over the one-to-one line demonstrates the consistency between the two independent decompositions.

and R_e adopted here are not big enough for parameter coupling in the fitting process to explain the observed trends.

3.1. The $M_{*,\text{sph}} - n_{\text{sph}}$ diagram

We find two different relations in the $M_{*,\text{sph}}-n_{\text{sph}}$ diagram (Figure 2) for the two morphological classes: ETGs and LTGs. Note that the (galaxy absolute magnitude, $\mathfrak{M}_{\text{gal}}$)- n relation for ETGs in Young & Currie (1994), Graham et al. (1996), Jerjen et al. (2000), Graham & Guzmán (2003), and Ferrarese et al. (2006) pertains to the whole galaxy, not the spheroidal component of the ETG (unless it is an elliptical galaxy). The $\mathfrak{M}_{\text{sph}}-n$ relation in Andredakis et al. (1995), Graham (2001), Khosroshahi et al. (2000), and Möllenhoff & Heidt (2001) pertains to the spheroid component of predominantly spiral galaxies.

The $M_{*,\text{sph}}-n_{\text{sph,maj}}$ relation that we derived for ETGs can be expressed as

$$\log(M_{*,\text{sph}}/M_{\odot}) = (3.27 \pm 0.25) \log(n_{\text{sph,maj}}/3) + (10.50 \pm 0.06), \quad (2)$$

with a total root mean square (rms) scatter of $\Delta_{\text{rms|sph}} = 0.46$ dex in the $\log(M_{*,\text{sph}})$ -direction. The intrinsic scatter and correlation coefficients for Equation 2 and all other relations presented in this paper are provided in Tables 1 and 2. As mentioned in Section 2, we used the BCES bisector regression that treats the ordinate and abscissa symmetrically. Additionally, using the

bisector line from the MPFITEXY regressions, we obtain the slope = 3.30 ± 0.18 and intercept = 10.50 ± 0.04 , which is closely consistent with the above relation obtained using the BCES regression. It should be noted that equation 2 is for spheroids, and is thus different from the (*Galaxy* mass, $M_{*,\text{gal}}$)-(galaxy Sérsic index) relation for ETG sample containing disk galaxies.

The bulges of LTGs follow a shallower relation which can be expressed as

$$\log(M_{*,\text{sph}}/M_{\odot}) = (1.31 \pm 0.22) \log(n_{\text{sph,maj}}/3) + (10.41 \pm 0.07), \quad (3)$$

with $\Delta_{\text{rms|sph}} = 0.32$ dex. The correlation of $M_{*,\text{sph}}$ with the equivalent axis Sérsic indices ($n_{\text{sph,eq}}$) for ETGs and LTGs are consistent with the above Equations 2 and 3, respectively, and are provided in Table 2. Equation 3 is also consistent with the relation obtained from the bisector MPFITEXY regression which provided the slope = 1.32 ± 0.19 and intercept = 10.41 ± 0.06 for LTGs. Similarly, for other correlations established in this paper, we have checked the best-fit lines using the MPFITEXY regression and these correlations with equivalent-axis bulge parameters are provided in the appendix Table A2.

Our $M_{*,\text{sph}}-n$ relations for ETGs and LTGs support the dual sequences seen in the spheroid luminosity (absolute magnitude)-(Sérsic index) diagram for ETGs and LTGs by Savorgnan (2016, and references therein), which was based on a sub-sample of our current sample. Importantly, our greater sample size has enabled a reduced uncertainty on the slope and intercept of the relations.

We also searched for substructures based on the other morphological information (core-Sérsic vs Sérsic galaxies, galaxies with a stellar disk versus galaxies without a stellar disk, and barred vs non-barred galaxies) and found no statistically significant division, except for a small difference between the best-fit lines for barred and non-barred galaxies (because the majority of our barred galaxies are LTGs)

Each of these relations implies that galaxies with greater spheroid stellar masses have higher spheroid Sérsic indices (Andredakis et al. 1995, their figure 5), i.e., a higher central stellar light concentration. Moreover, the $M_{*,\text{sph}}-n_{\text{sph}}$ relations with different slopes for the two morphological types (ETGs and LTGs) imply two different progressions of spheroid mass with the central light concentration. This might be reflecting two different ways the stellar mass evolves in the bulges of ETGs and LTGs. Hence, these distinct relations should be helpful for simulations and semi-analytic models studying the formation and evolution of galaxies with

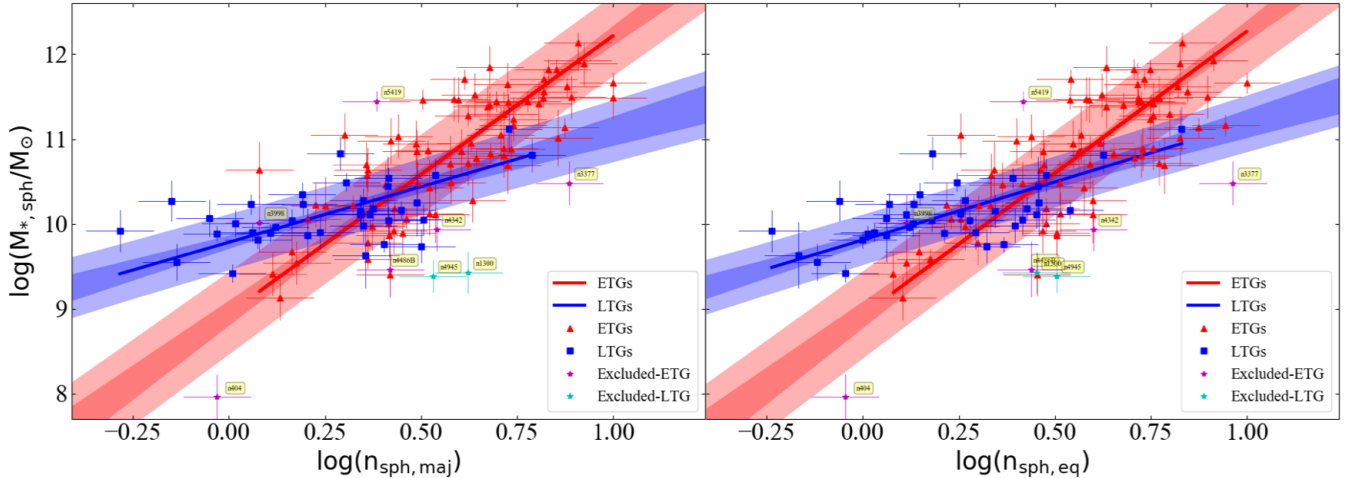


Figure 2. Spheroid mass versus major-axis (left panel) and equivalent-axis (right panel) Sérsic index describing the bulge/spheroidal component of the galaxies. In both panels, ETGs and LTGs are represented in red and blue, respectively. The bold red line for ETGs and blue line for LTGs represent the (symmetric) best-fit relations obtained using the BCES(BISECTOR) regression. The dark shaded region around these lines represents the $\pm 1\sigma$ uncertainty bound on the slopes and intercepts of these lines. The light-shaded region about these lines represent the $\pm 1\sigma$ scatter bound of the corresponding dataset. Both panels display the different $M_{*,\text{sph}}-n_{\text{sph}}$ relations defined by ETGs and LTGs (see Equations 2 and 3 for ETGs and LTGs, respectively). Galaxies excluded from our regressions, as discussed in Section 2, are marked in magenta and cyan. Additionally, excluding the two extreme right LTGs (blue data-points) still yields consistent relation within 1σ uncertainty bound of the $M_{*,\text{sph}}-n_{\text{sph}}$ relation for LTGs plotted here.

different morphology. We refrain from attempting a classical bulge versus pseudo-bulge classification. However, we note that no extra component for the (peanut shell)-shaped structure associated with a buckled bar (Combes et al. 1990; Athanassoula et al. 2015) is included in the galaxy decomposition because such features are effectively encapsulated by the B6 Fourier harmonic term (Ciambur 2016; Ciambur & Graham 2016; Ciambur et al. 2020) and the bar component of the decomposition. Inner discs are modelled as such.

3.2. The $M_{\text{BH}} - n_{\text{sph}}$ diagram

Obtaining the Sérsic index of a galactic spheroid is in some ways more straightforward than measuring its mass, or stellar velocity dispersion. This is because the Sérsic index can be obtained from the decomposition of the galaxy light even if the image is not photometrically calibrated. Whereas, measuring the spheroid stellar mass requires decomposition of a flux-calibrated image, which further requires the distance to the galaxy and an appropriate stellar mass-to-light ratio. Similarly, the stellar velocity dispersion measurement requires reducing and analyzing telescope-time-expensive spectra of the central stars of the galaxy.

The correlation between black hole mass and Sérsic index will, obviously, be beneficial for estimating the black hole mass of a galaxy using the Sérsic index of its spheroid (should it have one). Graham et al. (2003a)

were the first to establish a log-linear $M_{\text{BH}}-n_{\text{sph}}$ relation using a sample of 22 galaxies, which yielded $\log M_{\text{BH}} = (6.37 \pm 0.21) + (2.91 \pm 0.38) \log(n_{\text{sph}})$. It had a comparable rms scatter of $\Delta_{\text{rms}|_{\text{BH}}}=0.33$ dex with the contemporary $M_{\text{BH}}-\sigma$ relation ($\Delta_{\text{rms}|_{\text{BH}}}=0.31$ dex) of the day. Graham & Driver (2007a) subsequently advocated the log-quadratic relation $\log M_{\text{BH}} = (7.98 \pm 0.09) + (3.70 \pm 0.46) \log(n_{\text{sph}}/3) - (3.10 \pm 0.84)[\log n_{\text{sph}}/3]^2$, based on a sample of 27 galaxies. This resulted in a notably smaller intrinsic scatter (of just 0.18 dex) than that (0.31 dex) about their updated log-linear relation $\log M_{\text{BH}} = (7.81 \pm 0.08) + (2.69 \pm 0.28) \log(n_{\text{sph}}/3)$. In their log-quadratic $M_{\text{BH}}-n_{\text{sph}}$ relation, galaxies with smaller Sérsic indices resided on the steeper part of the curve, and galaxies with higher Sérsic indices defined a shallower part of the curve. This might have been an indication of two different relations for low- n_{sph} and high- n_{sph} galaxies that they were not able to see because of a small sample.

In consultation with the published literature, Savorgnan et al. (2013) doubled the sample size and derived the $M_{\text{BH}}-n_{\text{sph}}$ relations for Sérsic and core-Sérsic galaxies, however, the slopes of the two sub-samples were consistent within their $\pm 1\sigma$ uncertainty bound. Savorgnan (2016) subsequently used their own measurement of spheroid Sérsic index based on multi-component decompositions, to establish a single log-linear $M_{\text{BH}} \propto$

$n_{\text{sph}}^{(3.51 \pm 0.28)}$ relation, which was steeper than the relation reported by [Graham & Driver \(2007a\)](#). This is not surprising, as the slope from a single regression will vary arbitrarily according to the number of low- and high- n spheroids in one's sample. This difference in the $M_{\text{BH}}-n_{\text{sph}}$ relation was also because [Graham & Driver \(2007a\)](#) used the forward (Y over X) FITEXY regression routine from [Tremaine et al. \(2002\)](#), which minimized the scatter in the quantity to be predicted, i.e., M_{BH} , yielding a shallower slope for their $M_{\text{BH}}-n_{\text{sph}}$ relation. Though [Graham & Driver \(2007a\)](#) did not calculate the bisector/symmetric-fit relation using the FITEXY routine, the BCES bisector regression over their dataset yielded a slope of 2.85 ± 0.40 consistent with [Savorgnan \(2016\)](#)'s relation within the $\pm 1\sigma$ uncertainty bound. [Savorgnan \(2016\)](#) additionally explored the possibility of two different $M_{\text{BH}}-n_{\text{sph}}$ relations for ETGs and LTGs, however, due to just 17 LTGs in her sample, she could not find a statistically reliable best-fit line for the LTGs.

Here, we reinvestigate the $M_{\text{BH}}-n_{\text{sph}}$ relation, roughly doubling the sample size of 64 from [Savorgnan \(2016\)](#). Upon combining the latest $M_{\text{BH}}-M_{*,\text{sph}}$ relations for ETGs and LTGs from [Sahu et al. \(2019a\)](#) and [Davis et al. \(2019\)](#) with our $M_{*,\text{sph}}-n_{\text{sph}}$ relations defined by ETGs and LTGs (Equations 2 and 3), we expect $M_{\text{BH}} \propto n_{\text{sph}}^{4.15 \pm 0.39}$ and $M_{\text{BH}} \propto n_{\text{sph}}^{2.83 \pm 0.63}$ for ETGs and LTGs, respectively.

We started by performing a single symmetric regression between M_{BH} and n_{sph} for ETGs and LTGs combined (see Figure 3), which gives

$$\log(M_{\text{BH}}/M_{\odot}) = (3.79 \pm 0.23) \log(n_{\text{sph,maj}}/3) + (8.15 \pm 0.06), \quad (4)$$

between M_{BH} and $n_{\text{sph,maj}}$ with a total rms scatter of $\Delta_{\text{rms|BH}} = 0.69$ dex. Similarly, we obtained the single-regression relation between M_{BH} and $n_{\text{sph,eq}}$, presented in Table 2, which is closely consistent with the above $M_{\text{BH}}-n_{\text{sph,maj}}$ relation. Notably, this single-regression $M_{\text{BH}}-n_{\text{sph,maj}}$ relation is consistent with the [Savorgnan \(2016\)](#) relation within her larger $\pm 1\sigma$ error bound of the slope and intercept. The asymmetric BCES($M_{\text{BH}}|n$) regression for our total sample yields $M_{\text{BH}}-n_{\text{sph,maj}}^{(3.15 \pm 0.22)}$, which is still consistent with the relation observed in [Graham & Driver \(2007a\)](#), again, within the $\pm 1\sigma$ uncertainty limit of slopes. The intercept, however, has changed. This may partly be due to our use of ma-

ajorly $3.6 \mu\text{m}$ data while [Graham & Driver \(2007a\)](#) used R-band data¹⁰.

We further performed separate regressions for the ETGs and LTGs. The symmetric $M_{\text{BH}}-n_{\text{sph,maj}}$ relation defined by ETGs can be expressed as

$$\log(M_{\text{BH}}/M_{\odot}) = (3.95 \pm 0.34) \log(n_{\text{sph,maj}}/3) + (8.15 \pm 0.08), \quad (5)$$

with $\Delta_{\text{rms|BH}} = 0.65$ dex. The LTGs defined the shallower relation

$$\log(M_{\text{BH}}/M_{\odot}) = (2.85 \pm 0.31) \log(n_{\text{sph,maj}}/3) + (7.90 \pm 0.14), \quad (6)$$

with $\Delta_{\text{rms|BH}} = 0.67$ dex. The $M_{\text{BH}}-n_{\text{sph,maj}}$ and $M_{\text{BH}}-n_{\text{sph,eq}}$ relations obtained for ETGs versus LTGs are shown in the left- and right- hand panels of Figure 4, respectively. The $M_{\text{BH}}-n_{\text{sph,eq}}$ relations for ETGs and LTGs are consistent with the above $M_{\text{BH}}-n_{\text{sph,maj}}$ relations and are presented in Table 2. Importantly, the two relations for ETGs and LTGs in the $M_{\text{BH}}-n_{\text{sph,maj}}$ (and also in $M_{\text{BH}}-n_{\text{sph,eq}}$) diagram are consistent with the expected relations obtained after combining the $M_{\text{BH}}-M_{*,\text{sph}}$ and $M_{*,\text{sph}}-n_{\text{sph}}$ relations (as mentioned before) for ETGs and LTGs within the $\pm 1\sigma$ uncertainty bound.

We also performed multiple double regressions by dividing our sample into Sérsic versus core-Sérsic galaxies, galaxies with a disk (ES-, S0-, Sp-Types) versus galaxies without a disk (E-Type), and barred versus non-barred galaxies. In the former two cases, we did not find statistically different relations. Whereas, we see two slightly different $M_{\text{BH}}-n_{\text{sph}}$ lines for barred and non-barred galaxies because most of our LTGs are barred while most of our ETGs are non-barred. Moreover, the difference between the two relations followed by ETGs and LTGs is more prominent and consistent with the expected relations; hence, we conclude that the substructure in the $M_{\text{BH}}-n_{\text{sph}}$ diagram is due to ETG versus LTG categorization. Notably higher scatters around the $M_{\text{BH}}-n_{\text{sph}}$ relations depicted in Figure 4 obstruct the visibility of distinct relations for ETGs and LTGs, even though our statistical analysis suggests different relations. We reckon that, in future, a bigger data set will enable visibly distinct $M_{\text{BH}}-n_{\text{sph}}$ relations defined by ETGs and LTGs. For a comparison with the barred versus non-barred case, we also provide the $M_{\text{BH}}-n_{\text{sph,maj}}$ (and $M_{\text{BH}}-n_{\text{sph,eq}}$) relations obtained for the barred and non-barred galaxies along with the relations for ETGs and LTGs in Tables 1 and 2.

¹⁰ Many studies (e.g., [Kelvin et al. 2012](#); [Häufler et al. 2013](#); [Kennedy et al. 2016](#)) have quantified the dependence of galaxy Sérsic index on the wavelength band of image used.

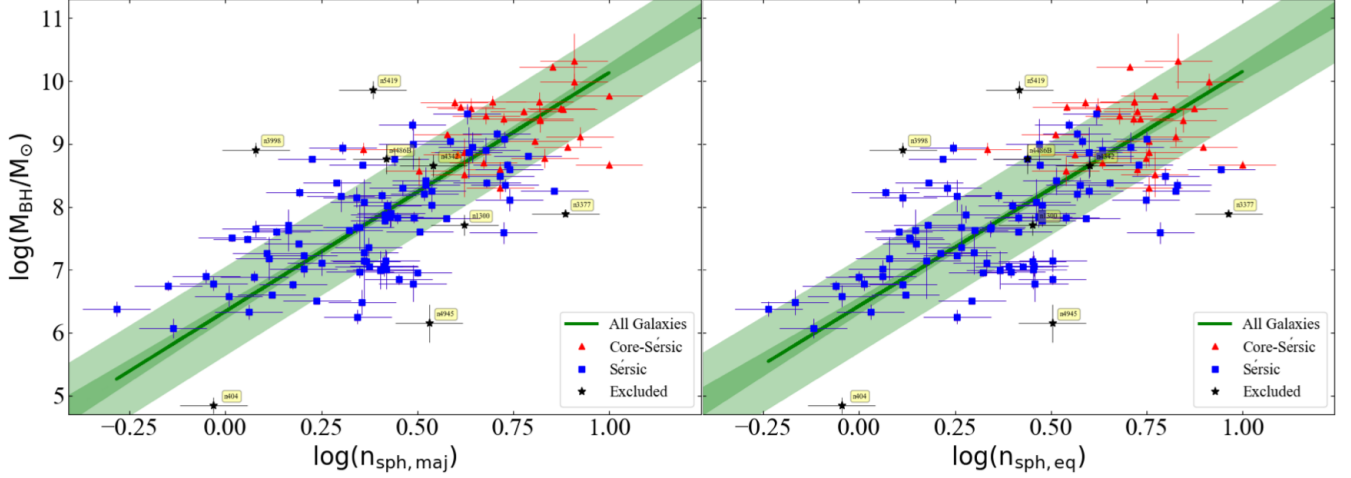


Figure 3. Black hole mass versus major-axis (left panel) and equivalent-axis (right panel) spheroid Sérsic index. Sérsic and core-Sérsic galaxies are shown in red and blue, respectively, and seem to follow the same single-regression $M_{\text{BH}}-n_{\text{sph}}$ relation.

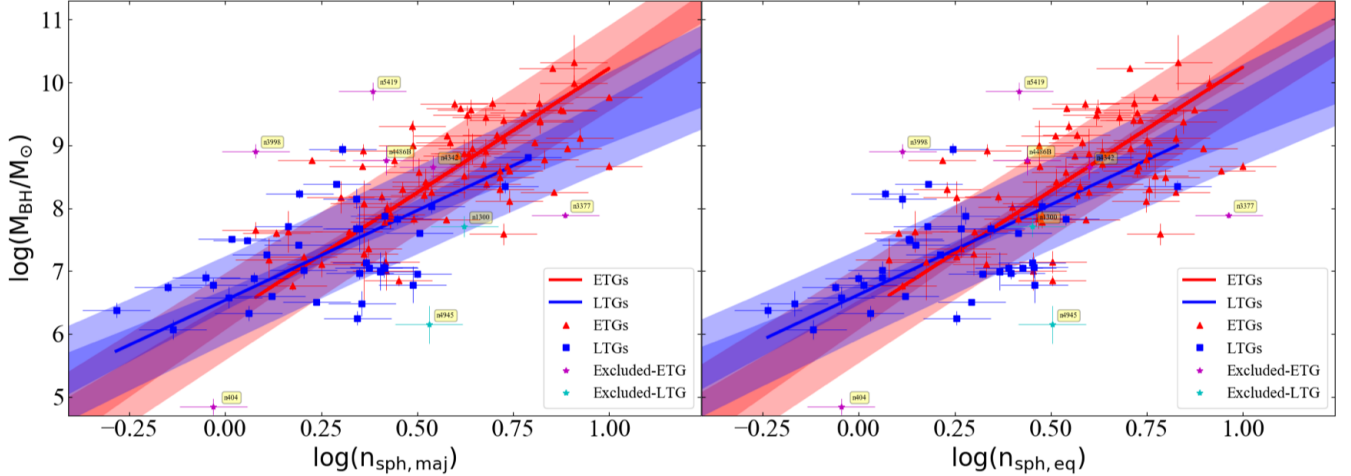


Figure 4. Similar to Figure 3, but now showing the separate regressions for ETGs and LTGs as expressed in Equations 5 and 6, respectively. These relations are consistent with the predicted $M_{\text{BH}}-n_{\text{sph}}$ relations obtained by combining the latest morphology-dependent $M_{\text{BH}}-M_{*,\text{sph}}$ relations (Davis et al. 2019; Sahu et al. 2019a) with the $M_{*,\text{sph}}-n_{\text{sph}}$ relations from Figure 2.

3.2.1. The M_{BH} -Concentration diagram

We also analyzed the relation between black hole mass and the light concentration of spheroids. Trujillo et al. (2001) quantified a central concentration index, for the light profile captured by a Sérsic function, as “a flux ratio” which can be expressed as $C(\alpha) = \gamma(2n, b_n \alpha^{1/n}) / \gamma(2n, b_n)$. Where, α is equal to r/R_e , and $0 < \alpha < 1$. For a particular α , a higher value of $C(\alpha)$ represents a spheroid or an elliptical galaxy with a greater central light or mass concentration.

To calculate the concentration index for our spheroids, we use the equivalent axis Sérsic index and the ex-

act value of b_n obtained using the equation $\Gamma(2n) = 2\gamma(2n, b_n)$. In Figure 5, we have plotted $C(\alpha)$ for our spheroids, for a range of α values, against their equivalent axis Sérsic indices, revealing how both quantities are related monotonically, as already seen in Trujillo et al. (2001).

Graham et al. (2001a) explored a range of values of α and found that $\alpha = 1/3$ produces a minimum scatter in the vertical direction in the $M_{\text{BH}}-C(\alpha)$ diagram. Moreover, for $\alpha > 0.5$ the range of concentration index values is so small that it becomes indistinguishable for different profile shapes (i.e., n), which is evident in our Figure 5, while low values of $\alpha (< 0.2)$ are not so practi-

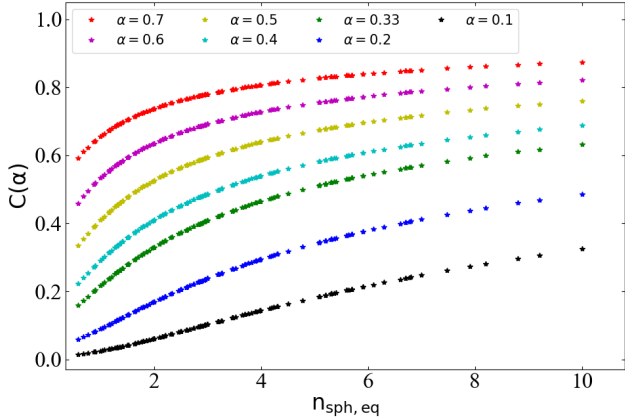


Figure 5. Central light concentration index plotted against equivalent axis Sérsic index for a range of α (fraction of effective half-light radius), representing the monotonicity between the concentration index and the Sérsic index. This plot also shows that for a high value of α ($\gtrsim 0.5$), the range of $C(\alpha)$ values is very small such that the increment in the $C(\alpha)$ with increasing n becomes minimal for $n \gtrsim 2$.

cal, especially for high redshift galaxies, as they require high spatial resolution [Graham et al. \(2001b\)](#). Therefore, in our investigation of the $M_{\text{BH}}-C(\alpha)$ relation, we use $C(\alpha)$ at $\alpha = 1/3$ for our spheroids. The uncertainty in $C(1/3)$ is calculated via error propagation based on a 20% uncertainty in the Sérsic index.

The correlation we obtained upon performing a symmetric regression between M_{BH} and $C(1/3)$ for the total (ETGs+LTGs) sample can be expressed as,

$$\log(M_{\text{BH}}/M_{\odot}) = (8.81 \pm 0.53) \log [C(1/3)/0.4] + (8.10 \pm 0.07). \quad (7)$$

with $\Delta_{\text{rms}|_{\text{BH}}} = 0.73$ dex in M_{BH} -direction. This is represented in Figure 6. This relation is steeper than the relation $M_{\text{BH}} \propto C(1/3)^{(6.81 \pm 0.95)}$ reported by [Graham et al. \(2001a\)](#) which was based on a set of only 21 galaxies.

Here, again, we looked for substructures due to Sérsic versus core-Sérsic galaxies, galaxies with a disk versus galaxies without a disk, barred versus non-barred galaxies, and ETGs versus LTGs. We find two slightly different relations only for the latter two cases, similar to the $M_{\text{BH}}-n_{\text{sph}}$ diagram, which is represented in Figure 7. Again, the substructure in the $M_{\text{BH}}-C(\alpha)$ diagram due to barred and non-barred galaxies is likely due to most of the LTGs being barred, while the dominant substructuring is due to the ETG and LTG morphology. The parameters of the $M_{\text{BH}}-C(1/3)$ relations defined by ETGs and LTGs are provided in Table 2. The best-fit lines ob-

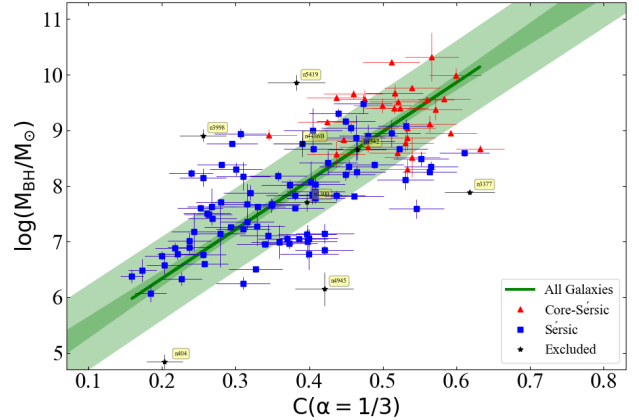


Figure 6. Black hole mass versus the spheroid’s central concentration index calculated using the equivalent-axis Sérsic index.

tained for the barred and non-barred galaxies are also provided in Table 2 for comparison.

3.3. The $M_{*,\text{sph}} - R_{\text{e},\text{sph}}$ diagram

There is a long history of studies which have worked on the galaxy size–luminosity ($L_{\text{gal}}-R_{\text{e},\text{gal}}$) relation for ETGs and found it to be curved (see [Graham 2019b](#), for a review). Here we explore the $M_{*,\text{sph}}-R_{\text{e},\text{sph}}$ diagram for the spheroids of ETGs and LTGs in our sample, for whom $R_{\text{e},\text{sph}}$ values were obtained from a careful image analysis.

Upon performing two different regressions for our ETGs and LTGs, we find a tight correlation between $M_{*,\text{sph}}$ and $R_{\text{e},\text{sph}}$ (see Figure 8) for both cases with remarkably smaller scatter ($\Delta_{\text{rms}|_{\text{sph}}} \sim 0.26$ dex) in the $M_{*,\text{sph}}$ -direction than the $M_{*,\text{sph}}-n_{\text{sph}}$ relations¹¹ (Equations 2 and 3 with $\Delta_{\text{rms}|_{\text{sph}}} = 0.46$ and 0.32 dex). The left- and right-hand panels in Figure 8 show the major-axis and equivalent-axis effective half-light radii ($R_{\text{e},\text{sph},\text{maj}}$ and $R_{\text{e},\text{sph},\text{eq}}$), respectively, on the horizontal-axes. The parameters for the $M_{*,\text{sph}}-R_{\text{e},\text{sph}}$ relations for both ETGs and LTGs are provided in Tables 1 (major-axis) and 2 (equivalent-axis).

The best-fit $M_{*,\text{sph}}-R_{\text{e},\text{sph}}$ lines for both ETGs and LTGs are log-linear and very close, such that their $\pm 1\sigma$ scatter region (shaded red and blue area in Figure 8) almost overlap with each other. Therefore, we further perform a single symmetric regression for our total

¹¹ The rms scatters in the horizontal direction for Equations 2, 3, and 8 are $\Delta_{\text{rms}|_n} = 0.14$ dex, $\Delta_{\text{rms}|_n} = 0.24$ dex, and $\Delta_{\text{rms}|_{R_e}} = 0.25$ dex, respectively.

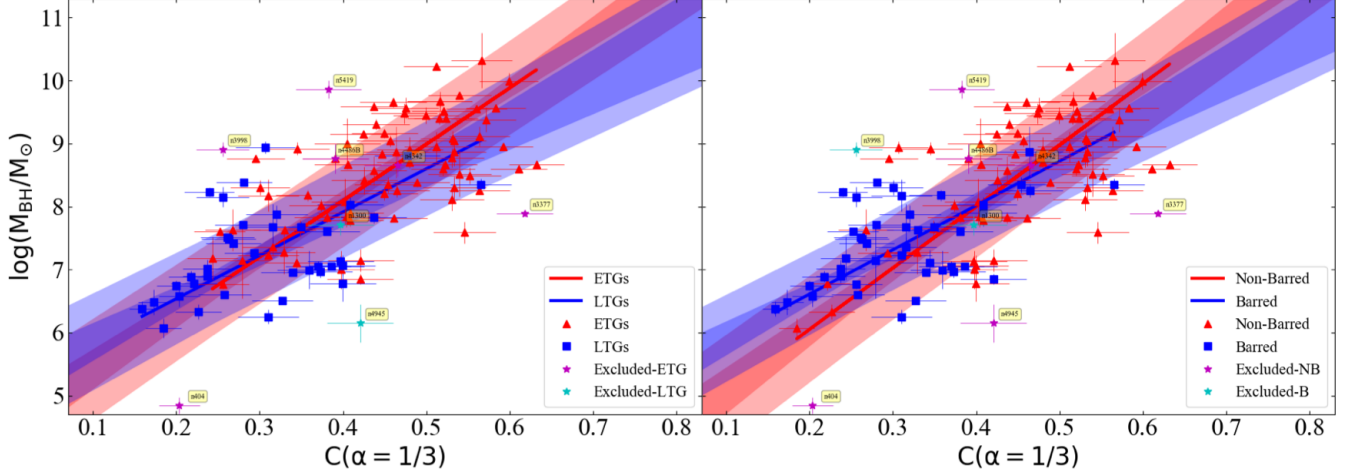


Figure 7. Similar to Figure 6, but now showing the best-fit lines obtained for ETGs and LTGs (left panel) plus barred and non-barred galaxies (right panel). The different lines obtained for barred and non-barred galaxies (right panel) is a consequence of most of our barred galaxies being LTGs.

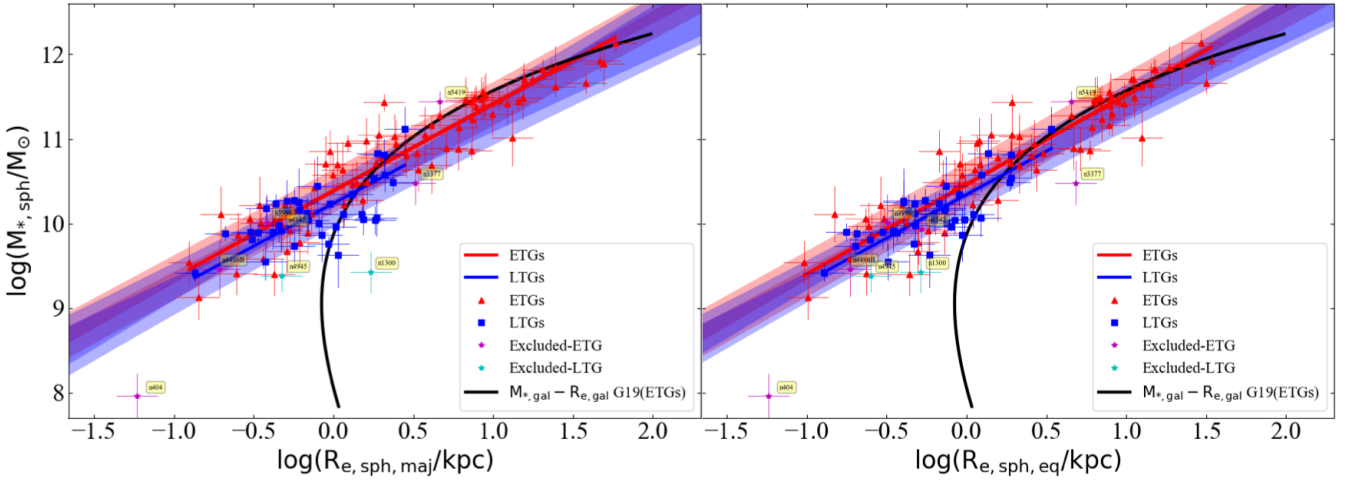


Figure 8. Spheroid stellar mass versus major-axis (left panel) and equivalent-axis (right panel) effective half-light radius of the spheroid. Both panels reveal that the spheroids of ETGs and LTGs follow closely consistent relations suggesting that a single $M_{*,\text{sph}}-R_{\text{e,sph}}$ relation (Equation 8) for all galaxy types is sufficient for the current data-set. The black curve is the $M_{*,\text{gal}}-R_{\text{e,gal}}$ relation for ETGs taken from [Graham \(2019b, their Figure 18\)](#) abbreviated as “G19”.

(ETG+LTG) sample, obtaining

$$\log(M_{*,\text{sph}}/M_{\odot}) = (1.08 \pm 0.04) \log(R_{\text{e,sph,maj}}/\text{kpc}) + (10.32 \pm 0.03), \quad (8)$$

with $\Delta_{\text{rms|sph}} = 0.27$ dex. This single-regression is represented in Figure 9, where the left-hand and right-hand panels show the $M_{*,\text{sph}}-R_{\text{e,sph,maj}}$ and $M_{*,\text{sph}}-R_{\text{e,sph,eq}}$ relations, respectively. The parameters for the single-regression $M_{*,\text{sph}}-R_{\text{e,sph,eq}}$ relation can be found in Table 2, which has consistent slope with the above $M_{*,\text{sph}}-R_{\text{e,sph,maj}}$ relation.

Our total (ETG+LTG) sample also includes some alleged pseudo-bulges, marked in Table-1 of [Sahu et al. \(2019b\)](#) along with their source of identification, suggesting that the above single \log -linear $M_{*,\text{sph}}-R_{\text{e,sph}}$ relation applies for both alleged pseudo-bulges and the normal/classical bulges.

For a comparison, we have plotted the $M_{*,\text{gal}}-R_{\text{e,gal}}$ curve for ETGs from [Graham \(2019b, their Figure 18\)](#) in our Figures 8 and 9. The shallower part of this curve, at the high mass (and size) end, seems to match well with our near-linear $M_{*,\text{sph}}-R_{\text{e,sph}}$ relation for bulges, however, the $R_{\text{e,sph}}$ of our spheroids becomes smaller

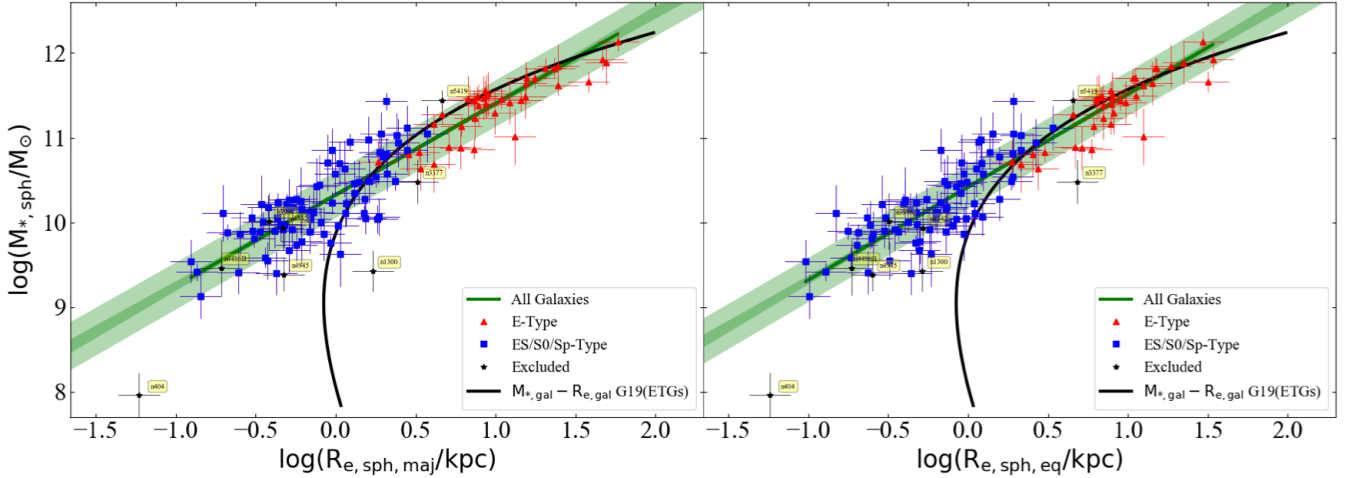


Figure 9. Similar to Figure 8, but now showing the single-regression $M_{*,sph}$ – $R_{e,sph}$ relation defined by the total (ETG+LTG) sample.

than their $R_{e,gal}$ at $\log(M_{*,sph}) \lesssim 10.5$ dex (or $R_e \lesssim 2$ kpc) due to the presence of disks enabling bigger $R_{e,gal}$ for their ETGs¹². We do not obtain a curved $M_{*,sph}$ – $R_{e,sph}$ relation, possibly, because our sample does not include many dwarf/low-mass ETGs or late-type spiral (Sc-, Sd-types) galaxies.

The bend-point of the curved L_{gal} – $R_{e,gal}$ relation for ETGs has been of past interest, because many studies have claimed that this bend-point is the point of distinction between dwarf elliptical (dE) and classical spheroids or (normal) elliptical galaxies (Sérsic 1968b; Kormendy et al. 2009; Fisher & Drory 2010, 2016). Different physical formation processes have been invoked for these alleged disjoint classes of galaxies (e.g., Tolstoy et al. 2009; Kormendy & Bender 2012; Somerville & Davé 2015). Providing a detailed investigation of this curved relation, Graham (2019b, their figure 4) present a (galaxy luminosity)– R_z diagram, where R_z represents the radius of the projected galaxy image enclosing $z\%$ of the total light, for z varying from 2% to 97%, including R_e for which $z=50\%$. Graham (2019b) find that all the $L_{B,gal}$ – $R_{z,gal}$ relations are curved but the location (the absolute magnitude) of the bend-point of each curve changes with z , revealing that the bend-point in the L – R_e (or $z=50\%$) relation has been used to artificially divide galaxies at a random magnitude based on the random percentage of light used to measure galaxy sizes.

Following Graham (2019b), using their Equation 22, we also calculated the radii containing $z = 10\%$ and

$z = 90\%$ of the spheroid’s light, i.e., $R_{10,sph}$ and $R_{90,sph}$, respectively. Figure 10 demonstrates how the spheroid stellar mass correlates with the equivalent axis radii $R_{10,sph,eq}$, $R_{50,sph,eq}$ (or $R_{e,sph,eq}$), and $R_{90,sph,eq}$, in the left, middle, and right panels, respectively. In all three cases, we find that ETGs and LTGs follow consistent relations suggesting a single $M_{*,sph}$ – $R_{z,sph}$ relation in each panel, however, the slope (and intercepts) of the relations change gradually with z . For comparison, we also show the $M_{*,gal}$ – $R_{z,gal}$ curves from Graham (2019b), which seem to agree well with the elliptical galaxies at the high mass end of our $M_{*,sph}$ – $R_{z,sph}$ relations. Whereas for galaxies with a disk (i.e., ES-, S0-, Sp-types), the radius containing $z\%$ of the spheroid’s light ($R_{z,sph}$) is smaller than the radius containing $z\%$ of whole galaxy’s light ($R_{z,gal}$). The parameters for the $M_{*,sph}$ – $R_{10,sph,eq}$ and $M_{*,sph}$ – $R_{90,sph,eq}$ relations are also provided in Table 2. Though for the range of our data-set we observe a (log)-linear relation between $M_{*,sph}$ and $R_{z,sph}$, addition of galaxies at the low-mass and small size end might reveal a curved $M_{*,sph}$ – $R_{z,sph}$ relation similar to the $M_{*,gal}$ – $R_{z,gal}$ curve for ETGs.

3.4. The M_{BH} – $R_{e,sph}$ diagram

Combining the M_{BH} – $M_{*,sph}$ relations defined by ETGs and LTGs, from Sahu et al. (2019a) and Davis et al. (2019), with the single-regression $M_{*,sph}$ – $R_{e,sph,maj}$ relation (Equation 8) followed by our combined sample of ETGs and LTGs, we expect $M_{BH} \propto R_{e,sph,maj}^{1.37 \pm 0.09}$ and $M_{BH} \propto R_{e,sph,maj}^{2.33 \pm 0.36}$ for ETGs and LTGs, respectively.

We first used a single regression for the total (ETG+LTG) sample, which yielded a good relation, provided in Tables 1 and 2 for the major- and equivalent-

¹² This is also partly intuitive because, for a given stellar density, a 2D disk (or a galaxy with a dominant disk) having the same total stellar mass as a 3D spheroidal distribution of stars will extend to a larger radii.

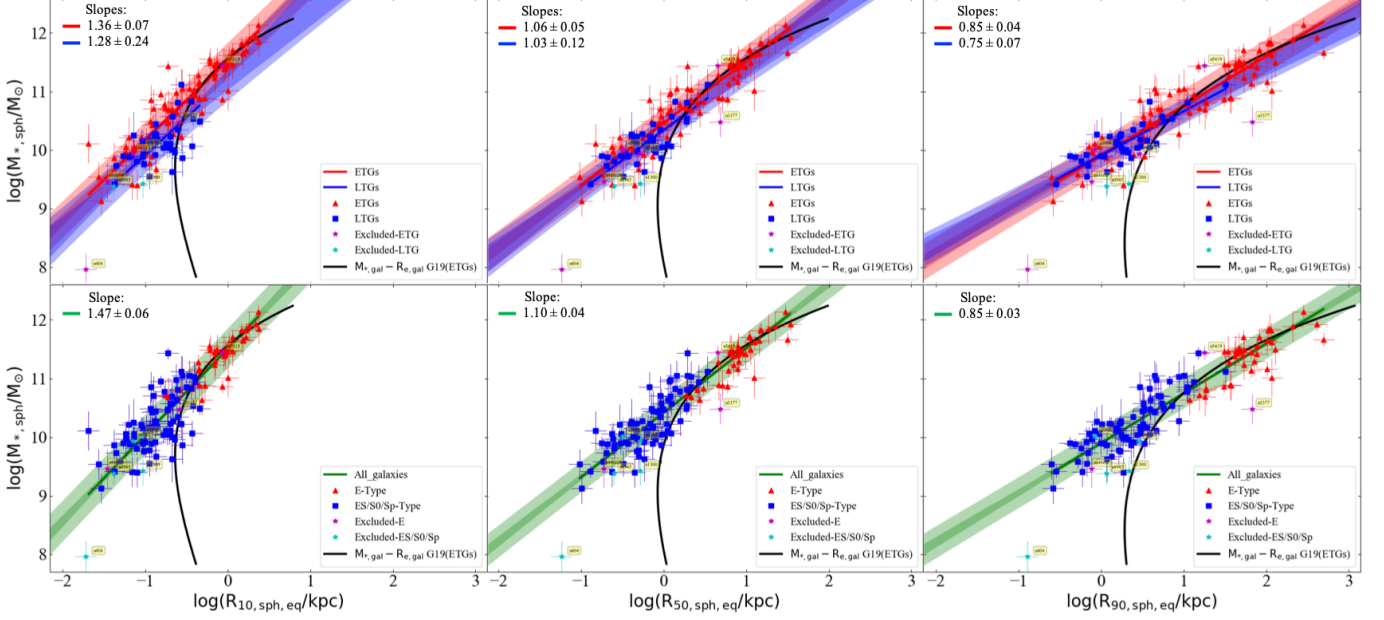


Figure 10. Similar to Figure 8 and 9, but now showing $R_{10,\text{sph,eq}}$, $R_{50,\text{sph,eq}}$ (or $R_{\text{e,sph,eq}}$), and $R_{90,\text{sph,eq}}$ on the horizontal axis in the left, middle, and right panels, respectively. Black curves are the $M_{*,\text{gal}} - R_{z,\text{gal}}$ curves from Graham (2019b) for the corresponding percentage (“z%”) of enclosed light. The top panels demonstrate that in all three cases ETGs and LTGs define consistent relations between $M_{*,\text{sph}}$ and $R_{z,\text{sph}}$ for the range of our sample, suggesting a single $M_{*,\text{sph}} - R_{z,\text{sph}}$ relation for the total (ETG+LTG) sample, presented in the bottom panels for each case. Importantly, the $M_{*,\text{sph}} - R_{z,\text{sph}}$ relations become shallower with increasing z . All the parameters for the $M_{*,\text{sph}} - R_{z,\text{sph}}$ relations are provided in Table 2.

axis $R_{\text{e,sph}}$, respectively, but with a higher scatter than the soon to be revealed separate relations for ETGs and LTGs. Moreover, it is inconsistent with the above prediction of the two relations in the $M_{\text{BH}} - R_{\text{e,sph}}$ diagram.

Upon performing separate regressions for ETGs and LTGs in the $M_{\text{BH}} - R_{\text{e,sph}}$ diagram, we do find two different relations for the two morphological classes. These relations are presented in Figure 11 with the left-hand and right-hand panels displaying $R_{\text{e,sph,maj}}$ and $R_{\text{e,sph,eq}}$, respectively. The relation defined by all ETGs can be expressed as,

$$\log(M_{\text{BH}}/M_{\odot}) = (1.26 \pm 0.08) \log(R_{\text{e,sph,maj}}/\text{kpc}) + (8.00 \pm 0.07), \quad (9)$$

with $\Delta_{\text{rms|BH}} = 0.58$ dex, while LTGs define the relation

$$\log(M_{\text{BH}}/M_{\odot}) = (2.33 \pm 0.31) \log(R_{\text{e,sph,maj}}/\text{kpc}) + (7.54 \pm 0.10), \quad (10)$$

with $\Delta_{\text{rms|BH}} = 0.62$ dex. The slope of the $M_{\text{BH}} - R_{\text{e,sph,eq}}$ relations for ETGs and LTGs are consistent with the corresponding $M_{\text{BH}} - R_{\text{e,sph,maj}}$ relations, and their fit parameters are provided in Table 2. These two relations (Equations 9 & 10) for ETGs and LTGs are in agreement with the expected $M_{\text{BH}} - R_{\text{e,sph}}$ relations mentioned at the beginning of this sub-section. Additionally, we note that our $M_{\text{BH}} - R_{\text{e,sph,maj}}$ relation for

ETGs is also consistent with the relation obtained by de Nicola et al. (2019), based on an ETG-dominated sample.

Each of our non-linear, but log-linear, $M_{\text{BH}} - R_{\text{e,sph}}$ relations reveal that galaxies with more massive black holes tend to have a larger (bulge) half-light radii. However, the two different slopes of the $M_{\text{BH}} - R_{\text{e,sph}}$ relations for ETGs and LTGs suggest that the process of evolution between black hole mass and spheroid size ($R_{\text{e,sph}}$), which further relates to the spheroid stellar mass, tends to be different for these different morphological types. This also supports our morphology-dependent $M_{\text{BH}} - M_{*,\text{sph}}$, and $M_{\text{BH}} - M_{*,\text{gal}}$ relations (Davis et al. 2018; Sahu et al. 2019a), where ETGs and LTGs are found to follow two different relations. The total rms scatter about the $M_{\text{BH}} - R_{\text{e,sph}}$ relation is smaller than the total rms scatter about the $M_{\text{BH}} - M_{*,\text{sph}}$ relation for LTGs (cf. $\Delta_{\text{rms|BH}} = 0.64$ dex), whereas, for ETGs it is a bit higher about the $M_{\text{BH}} - R_{\text{e,sph}}$ relation (cf. $\Delta_{\text{rms|BH}} = 0.52$ dex about the $M_{\text{BH}} - M_{*,\text{sph}}$ relation).

We did not find significantly different relations upon dividing our total sample into Sérsic versus core-Sérsic galaxies, or barred versus non-barred galaxies, in the $M_{\text{BH}} - R_{\text{e,sph}}$ diagram. However, when we perform separate regressions for ETGs with a stellar disk (ES-, and S0-types) and ETGs without a stellar disk (E-type), we find two almost parallel relations which are offset

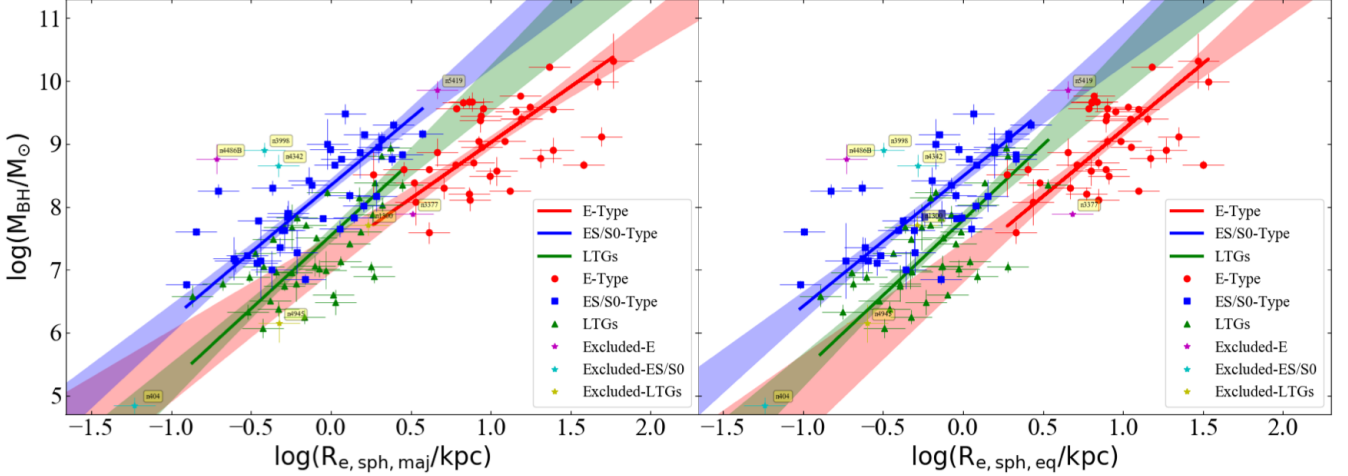


Figure 13. Similar to Figure 12, but now also showing the $M_{\text{BH}}-R_{\text{e,sph}}$ relation defined by LTGs in the same diagram. Just for clarity, we are not showing the (light-shaded) 1σ scatter regions, which are visible in Figures 11 and 12.

In passing, we note that the $M_{\text{BH}}-R_{\text{e,sph}}$ relation that we obtained for ETGs without a disk (elliptical galaxies)—most of which are core-Sérsic galaxies—is also consistent with the relation $M_{\text{BH}} \propto R_{\text{e}}^{1.86 \pm 0.26}$ obtained by combining the $M_{\text{BH}}-(\text{break radius or depleted core radius, } R_{\text{b}})$ and $R_{\text{b}}-R_{\text{e}}$ relations observed for cored galaxies in [Dullo & Graham \(2014\)](#).

This offset between ETGs with and without a disk in the $M_{\text{BH}}-R_{\text{e,sph}}$ diagram is analogous to the offset found between the parallel relations for ETGs with and without a disk in the $M_{\text{BH}}-M_{*,\text{sph}}$ diagram ([Sahu et al. 2019a](#), their figure 8). Also, on combining the $M_{\text{BH}}-M_{*,\text{sph}}$ relations defined by ETGs with and without a disk ([Sahu et al. 2019a](#), their Equations 12 and 13), with our $M_{*,\text{sph}}-R_{\text{e,sph}}$ relation (Equation 8), we obtain $M_{\text{BH}} \propto R_{\text{e,sph,maj}}^{2.01 \pm 0.23}$ and $M_{\text{BH}} \propto R_{\text{e,sph,maj}}^{2.05 \pm 0.23}$ ($M_{\text{BH}} \propto R_{\text{e,sph,eq}}^{2.05 \pm 0.23}$ and $M_{\text{BH}} \propto R_{\text{e,sph,eq}}^{2.09 \pm 0.23}$, for $R_{\text{e,sph,eq}}$), which are consistent with the observed relations for ETGs with a disk and ETGs without a disk, respectively (Equation 11 & 12, see Table 2 for $M_{\text{BH}} - R_{\text{e,sph,eq}}$ parameters).

Importantly, as mentioned in [Sahu et al. \(2019a\)](#), this order of magnitude offset has little to do with the black hole masses of these two categories. Qualitatively, this offset can be understood by the different sizes of the spheroid effective half-light radius corresponding to ETGs with a disk (ES and S0) and ETGs without a disk (E). The elliptical (ES) and lenticular (S0) galaxies, which have intermediate/large-scale stellar disks in addition to their spheroids, have a smaller $R_{\text{e,sph}}$ relative to the elliptical galaxies which are comprised (almost) entirely of spheroids. This difference in $R_{\text{e,sph}}$ between the two sub-populations of ETGs creates the offset between the $M_{\text{BH}}-R_{\text{e,sph}}$ relations defined by them, and

because of the non-zero slope of the $M_{\text{BH}}-R_{\text{e,sph}}$ relations, we see an offset in the vertical direction.

The relation $M_{*,\text{sph}} = (M/L)2\pi R_{\text{e}}^2 \langle I \rangle_{\text{e}}$ (e.g. Equation 8 in [Graham 2019b](#)), where (M/L) represents the stellar mass-to-light ratio and $\langle I \rangle_{\text{e}}$ is the averaged intensity within R_{e} , suggests that $\log(M_{*,\text{sph}}) \propto \log(\langle I \rangle_{\text{e}}) + 2 \log(R_{\text{e}})$, for a constant mass-to-light ratio. This can help us quantitatively understand the origin of the offset (of 1.12 ± 0.20 dex) found in the $\log(M_{\text{BH}})-\log(M_{*,\text{sph}})$ diagram ([Sahu et al. 2019a](#), their section 4.2) between ETGs with and without a stellar disk. We find a vertical offset of 1.41 ± 0.23 dex between the two sub-samples of ETGs in the $\log(M_{\text{BH}})-2 \log(R_{\text{e,sph,eq}})$ diagram. Whereas, we do not find separate statistically significant $\log(M_{\text{BH}})-\log(\langle I \rangle_{\text{e}})$ relations for these two populations, implying a single $\log(M_{\text{BH}})-\log(\langle I \rangle_{\text{e}})$ for ETGs with and without a disk. This suggests that the offset observed in the $\log(M_{\text{BH}})-\log(M_{*,\text{sph}})$ diagram by [Sahu et al. \(2019a\)](#) originates mainly from the offset in the $\log(M_{\text{BH}})-\log(R_{\text{e,sph}})$ diagram.

Furthermore, in the plot of M_{BH} versus the effective radius of the whole galaxy ($R_{\text{e,gal}}$), this offset is expected to disappear, such that all the ETGs will follow a single $M_{\text{BH}}-R_{\text{e,gal}}$ relation, analogous to the combined behaviour of ETGs with and without a disk in the $M_{\text{BH}}-M_{*,\text{gal}}$ diagram ([Sahu et al. 2019a](#), see the right-hand panel of their Figure 8), where the two sub-populations of ETGs follow consistent $M_{\text{BH}}-M_{*,\text{gal}}$ relations.

Similar to the previous subsection, here also we investigate the correlations of black hole mass with radii containing $z = 10\%$ and $z = 90\%$ of the spheroid’s total light, in addition to the 50% ($R_{\text{e,sph}}$) radius discussed above. Figure 14 presents the correlations we observed between black hole mass and $R_{10,\text{sph,eq}}$, $R_{50,\text{sph,eq}}$ (or

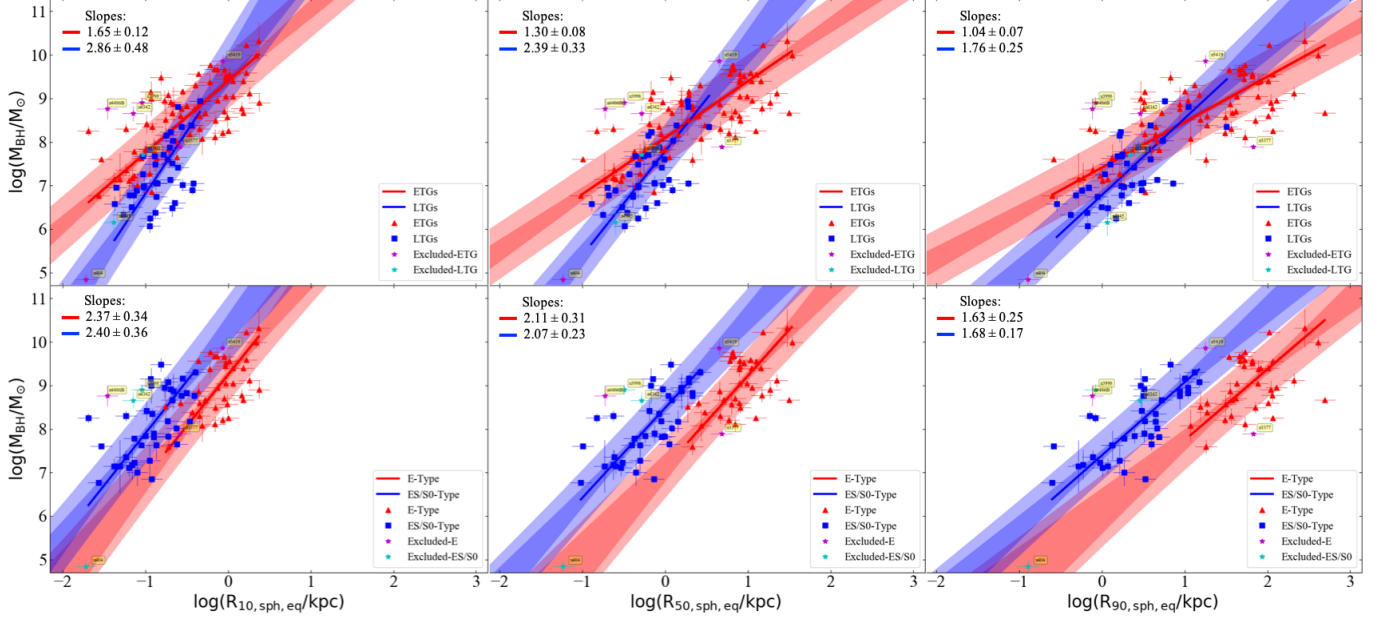


Figure 14. Similar to Figure 11 and 12, but now also showing the correlations of M_{BH} with the radius containing $z = 10\%$ ($R_{10, \text{sph, eq}}$) and $z = 90\%$ ($R_{90, \text{sph, eq}}$) of the spheroid’s light in the left and right panels, in addition to $M_{\text{BH}}-R_{e, \text{sph, eq}}$ relations in the middle panel. Top panels reveal that ETGs and LTGs follow two different relations in all three cases. The bottom panel reveals that the offset between ETGs with and without a disk is obtained in all cases, where the offset varies with z . Additionally, due to the more massive systems having larger Sérsic indices, for all sub-morphologies the slope of the $M_{\text{BH}}-R_{z, \text{sph, eq}}$ relation gradually decreases with increasing z . Intercepts and the scatter about these relations can be found in Table 2.

$R_{e, \text{sph, eq}}$), and $R_{90, \text{sph, eq}}$, respectively in the left, middle, and right panels. The top panels show that ETGs and LTGs define two different $M_{\text{BH}}-R_{z, \text{sph, eq}}$ relations irrespective of z , however, the slopes of the relations become shallower with increasing z . The bottom panels reveal that the offset between the $M_{\text{BH}}-R_{z, \text{sph, eq}}$ rela-

tions followed by ETGs with a disk and ETGs without a disk are found in all cases; however, as expected, the amount of the offset varies with z and also the slopes of these relations become shallower with increasing z . The parameters for the $M_{\text{BH}}-R_{z, \text{sph, eq}}$ relations obtained for $z = 10\%$ and $z = 90\%$ are also presented in Table 2.

Table 1. Correlations of $M_{*, \text{sph}}$ and M_{BH} with the bulge/spheroid major-axis properties ($n_{\text{sph, maj}}$ and $R_{e, \text{sph, maj}}$)

Category	Number	α	β	ϵ	Δ_{rms}	r	$\log p$	r_s	$\log p_s$
(1)	(2)	(3)	(4)	(5)	(6)	(7)	(8)	(9)	(10)
$\log(M_{*, \text{sph}}/M_{\odot}) = \alpha \log(n_{\text{sph, maj}}/3) + \beta$									
ETGs	77	3.27 ± 0.25	10.50 ± 0.06	0.27	0.46	0.79	-17.14	0.80	-17.32
LTGs	38	1.31 ± 0.22	10.41 ± 0.07	0.23	0.32	0.54	-3.28	0.41	-2.01
$\log(M_{\text{BH}}/M_{\odot}) = \alpha \log(n_{\text{sph, maj}}/3) + \beta$									
All Galaxies	115	3.79 ± 0.23	8.15 ± 0.06	0.60	0.69	0.77	-22.85	0.76	-22.36
ETGs	77	3.95 ± 0.34	8.15 ± 0.08	0.54	0.65	0.71	-12.46	0.69	-11.42
LTGs	38	2.85 ± 0.31	7.90 ± 0.14	0.62	0.67	0.53	-3.20	0.45	-2.36
Non-Barred	71	3.89 ± 0.31	8.15 ± 0.10	0.61	0.70	0.72	-11.80	0.64	-8.61
Barred	44	3.08 ± 0.36	8.00 ± 0.11	0.55	0.61	0.54	-3.76	0.47	-2.95
$\log(M_{*, \text{sph}}/M_{\odot}) = \alpha \log(R_{e, \text{sph, maj}}) + \beta$									

Table 1 continued

Table 1 (*continued*)

Category	Number	α	β	ϵ	Δ_{rms}	r	$\log p$	r_s	$\log p_s$
			dex	dex	dex		dex		dex
(1)	(2)	(3)	(4)	(5)	(6)	(7)	(8)	(9)	(10)
All Galaxies	115	1.08 ± 0.04	10.32 ± 0.03	0.13	0.27	0.92	-47.92	0.90	-42.83
ETGs	77	1.03 ± 0.05	10.39 ± 0.04	0.09	0.25	0.93	-34.73	0.94	-36.98
LTGs	38	1.01 ± 0.15	10.24 ± 0.05	0.16	0.27	0.66	-5.26	0.58	-3.84
$\log(M_{\text{BH}}/M_{\odot}) = \alpha \log(R_{\text{e,sph,maj}}) + \beta$									
ETGs with a disk	39	2.13 ± 0.22	8.34 ± 0.09	0.47	0.55	0.74	-7.21	0.76	-7.81
ETGs without a disk	38	1.78 ± 0.24	7.24 ± 0.25	0.55	0.60	0.55	-3.45	0.52	-3.13
ETGs (All)	77	1.26 ± 0.08	8.00 ± 0.07	0.54	0.58	0.76	-15.10	0.74	-13.95
LTGs	38	2.33 ± 0.31	7.54 ± 0.10	0.54	0.62	0.63	-4.66	0.62	-4.43
All Galaxies	115	1.59 ± 0.09	7.73 ± 0.07	0.63	0.67	0.78	-23.56	0.78	-24.26

NOTE— Columns: (1) Subclass of galaxies. (2) Number of galaxies in a subclass. (3) Slope of the line obtained from the BCES(BISECTOR) regression. (4) Intercept of the line obtained from the BCES(BISECTOR) regression. (5) Intrinsic scatter in the vertical ($\log M_{*,\text{sph}}$ or $\log M_{\text{BH}}$)-direction (see Equation 1 from [Graham & Driver 2007a](#)). (6) Total root mean square (rms) scatter in the vertical direction. (7) Pearson correlation coefficient. (8) Pearson correlation probability value. (9) Spearman rank-order correlation coefficient. (10) Spearman rank-order correlation probability value.

Table 2. Correlations of $M_{*,\text{sph}}$ and M_{BH} with the bulge/spheroid equivalent-axis properties ($n_{\text{eq,sph}}$, $C(1/3)$, $R_{\text{e,sph,eq}}$, $R_{10,\text{sph,eq}}$, and $R_{90,\text{sph,eq}}$)

Category	Number	α	β	ϵ	Δ_{rms}	r	$\log p$	r_s	$\log p_s$
			dex	dex	dex		dex		dex
(1)	(2)	(3)	(4)	(5)	(6)	(7)	(8)	(9)	(10)
$\log(M_{*,\text{sph}}/M_{\odot}) = \alpha \log(n_{\text{sph,eq}}/3) + \beta$									
ETGs	77	3.34 ± 0.24	10.52 ± 0.06	0.32	0.49	0.77	-15.63	0.74	-13.86
LTGs	38	1.37 ± 0.20	10.46 ± 0.07	0.20	0.28	0.63	-4.61	0.55	-3.39
$\log(M_{\text{BH}}/M_{\odot}) = \alpha \log(n_{\text{sph,eq}}/3) + \beta$									
All Galaxies	115	3.72 ± 0.23	8.20 ± 0.07	0.65	0.73	0.74	-20.14	0.74	-20.22
ETGs	77	3.94 ± 0.37	8.18 ± 0.09	0.63	0.73	0.64	-9.37	0.60	-8.13
LTGs	38	2.86 ± 0.33	7.99 ± 0.16	0.64	0.68	0.49	-2.78	0.50	-2.86
Non-Barred	71	4.20 ± 0.38	8.11 ± 0.10	0.69	0.79	0.64	-8.89	0.54	-5.88
Barred	44	2.91 ± 0.30	8.08 ± 0.13	0.56	0.61	0.52	-3.54	0.45	-2.66
$\log(M_{\text{BH}}/M_{\odot}) = \alpha C(1/3)/0.4 + \beta$									
All Galaxies	115	8.81 ± 0.53	8.10 ± 0.07	0.65	0.73	0.74	-20.16	0.74	-20.17
ETGs	77	8.94 ± 0.86	8.10 ± 0.09	0.63	0.72	0.64	-9.45	0.60	-8.13
LTGs	38	6.88 ± 0.97	7.91 ± 0.16	0.64	0.68	0.47	-2.57	0.50	-2.83
Non-Barred	71	9.75 ± 0.93	8.00 ± 0.11	0.70	0.79	0.64	-8.77	0.54	-5.88
Barred	44	7.03 ± 0.88	8.02 ± 0.13	0.56	0.61	0.51	-3.36	0.45	-2.63
$\log(M_{*,\text{sph}}/M_{\odot}) = \alpha \log(R_{\text{e,sph,eq}}) + \beta$									
All Galaxies	115	1.10 ± 0.04	10.42 ± 0.03	0.08	0.26	0.93	-50.60	0.92	-46.02
ETGs	77	1.06 ± 0.05	10.46 ± 0.04	0.08	0.26	0.93	-33.85	0.94	-35.31
LTGs	38	1.03 ± 0.12	10.34 ± 0.05	0.00	0.22	0.78	-7.98	0.67	-5.39
$\log(M_{\text{BH}}/M_{\odot}) = \alpha \log(R_{\text{e,sph,eq}}) + \beta$									
ETGs with a disk	39	2.07 ± 0.23	8.49 ± 0.09	0.52	0.59	0.70	-6.19	0.71	-6.33

Table 2 *continued*

Table 2 (continued)

Category	Number	α	β	ϵ	Δ_{rms}	r	$\log p$	r_s	$\log p_s$
			dex	dex	dex		dex		dex
(1)	(2)	(3)	(4)	(5)	(6)	(7)	(8)	(9)	(10)
ETGs without a disk	38	2.11 ± 0.31	7.11 ± 0.27	0.55	0.61	0.53	-3.27	0.46	-2.43
ETGs	77	1.30 ± 0.08	8.10 ± 0.07	0.56	0.60	0.75	-14.41	0.72	-12.76
LTGs	38	2.39 ± 0.33	7.79 ± 0.13	0.52	0.60	0.66	-5.13	0.66	-5.21
All Galaxies	115	1.62 ± 0.09	7.86 ± 0.06	0.62	0.67	0.78	-23.81	0.78	-24.29
$\log(M_{*,\text{sph}}/M_{\odot}) = \alpha \log(R_{10,\text{sph,eq}}) + \beta$									
All Galaxies	115	1.47 ± 0.06	11.51 ± 0.04	0.17	0.33	0.88	-38.55	0.86	-34.27
$\log(M_{\text{BH}}/M_{\odot}) = \alpha \log(R_{10,\text{sph,eq}}) + \beta$									
ETGs with a disk	39	2.39 ± 0.36	10.30 ± 0.32	0.60	0.68	0.61	-4.38	0.63	-4.78
ETGs without a disk	38	2.37 ± 0.34	9.25 ± 0.10	0.53	0.61	0.54	-3.37	0.47	-2.54
ETGs	77	1.65 ± 0.12	9.40 ± 0.09	0.56	0.62	0.73	-13.50	0.71	-12.24
LTGs	38	2.86 ± 0.47	9.67 ± 0.44	0.60	0.69	0.54	-3.30	0.50	-2.83
$\log(M_{*,\text{sph}}/M_{\odot}) = \alpha \log(R_{90,\text{sph,eq}}) + \beta$									
All Galaxies	115	0.85 ± 0.03	9.90 ± 0.03	0.12	0.26	0.93	-50.53	0.92	-47.05
$\log(M_{\text{BH}}/M_{\odot}) = \alpha \log(R_{90,\text{sph,eq}}) + \beta$									
ETGs with a disk	39	1.68 ± 0.17	7.40 ± 0.13	0.51	0.56	0.73	-6.89	0.71	-6.35
ETGs without a disk	38	1.63 ± 0.25	6.11 ± 0.42	0.61	0.63	0.47	-2.52	0.41	-1.95
ETGs	77	1.04 ± 0.07	7.41 ± 0.09	0.58	0.60	0.74	-14.09	0.71	-12.17
LTGs	38	1.76 ± 0.25	6.78 ± 0.10	0.54	0.58	0.67	-5.30	0.68	-5.50

NOTE—Column names are same as Table 1.

4. SUMMARY

We have used the largest sample of galaxies to date with directly-measured black hole masses, and carefully measured bulge parameters obtained from multi-component decomposition of their galaxy light in our previous studies (Savorgnan & Graham 2016; Davis et al. 2019; Sahu et al. 2019a). Using this extensive data-set, we have investigated the correlations between black hole mass (M_{BH}) and the bulge Sérsic index (n_{sph}), bulge central light concentration index (C), and the bulge effective half-light radius ($R_{\text{e,sph}}$).

For our sample, we also investigated the correlations between bulge mass ($M_{*,\text{sph}}$) and both the bulge Sérsic index and bulge half-light radius. We then combined these with the latest $M_{\text{BH}}-M_{*,\text{sph}}$ relations to predict and check upon the observed correlations of M_{BH} with n_{sph} and $R_{\text{e,sph}}$.

In all of the relations we investigated, we explored the possibility of substructure due to various subcategories of galaxy morphology, i.e., Sérsic versus core-Sérsic galaxies, galaxies with a stellar disk versus galaxies without a stellar disk, barred versus non-barred galaxies, and ETGs versus LTGs.

Parameters for all the correlations presented in this paper are separately listed in Table 1 and Table 2. The

slope of the correlations that we obtained for M_{BH} or $M_{*,\text{sph}}$ with the major-axis bulge parameters ($n_{\text{sph,maj}}$ and $R_{\text{e,sph,maj}}$) are consistent with the slope from the corresponding correlations of M_{BH} or $M_{*,\text{sph}}$ with the equivalent-axis bulge parameters ($n_{\text{sph,eq}}$ and $R_{\text{e,sph,eq}}$).

Our prime results can be summarized as follows,

- ETGs and LTGs follow two different $M_{*,\text{sph}}-n_{\text{sph}}$ relations (see Figure 2), with slopes equal to 3.27 ± 0.25 and 1.31 ± 0.22 , and total rms scatter equal to $\Delta_{\text{rms}|_{\text{sph}}}=0.46$ dex and 0.32 dex, respectively (Equations 2 and 3), in the $M_{*,\text{sph}}-n_{\text{sph,maj}}$ diagram. As the Sérsic index is a measure of the central concentration of a bulge’s light, these different slopes for the $M_{*,\text{sph}}-n_{\text{sph}}$ relation suggest distinct mechanisms for the evolution of spheroid mass and central light (or stellar mass) concentration in ETGs and LTGs.
- In the $M_{\text{BH}}-n_{\text{sph}}$ diagram, ETGs and LTGs seem to follow two different relations with $M_{\text{BH}} \propto n_{\text{sph,maj}}^{3.95 \pm 0.34}$ and $M_{\text{BH}} \propto n_{\text{sph,maj}}^{2.85 \pm 0.31}$ with $\Delta_{\text{rms}|_{\text{BH}}} = 0.65$ dex and 0.67 dex, respectively (Figure 4, Equations 5 and 6).
- In the diagram showing the black hole mass versus the spheroid central concentration index, $C(1/3)$,

we again find two (slightly) different relations due to ETGs and LTGs (Figure 7, Table 2), analogous to the $M_{\text{BH}}-n_{\text{sph}}$ diagram. The slopes for the $M_{\text{BH}}-C(1/3)$ relations are 8.94 ± 0.86 and 6.88 ± 0.97 with $\Delta_{\text{rms}|_{\text{BH}}}=0.72$ dex and 0.68 dex, respectively, for ETGs and LTGs.

- We find a tight near-linear relation between $M_{*,\text{sph}}$ and $R_{\text{e,sph}}$ for our range of data (Figures 8 and 9). Both ETGs and LTGs define the log-linear relation $M_{*,\text{sph}} \propto R_{\text{e,sph,maj}}^{1.08 \pm 0.04}$ (Equation 8) with $\Delta_{\text{rms}|_{\text{sph}}}=0.27$ dex. An extended view of the $M_{*,\text{gal}}-R_{\text{e,gal}}$ relation for ETGs is curved (Graham 2019b), and our $M_{*,\text{sph}}-R_{\text{e,sph}}$ relation, somewhat dominated by massive spheroids, agrees with the quasi-linear part of the curve at high-masses where E-type galaxies dominate.
- ETGs and LTGs define two different relations between black hole mass and bulge R_{e} (Figure 11), such that $M_{\text{BH}}-R_{\text{e,sph,maj}}^{(1.26 \pm 0.08)}$ and $M_{\text{BH}}-R_{\text{e,sph,maj}}^{(2.33 \pm 0.31)}$ for ETGs and LTGs, with $\Delta_{\text{rms}|_{\text{BH}}}=0.58$ dex and 0.62 dex, respectively (Equation 9 and 10). This is analogous to the substructure in the $M_{\text{BH}}-M_{*,\text{sph}}$ diagram due to ETGs and LTGs (Sahu et al. 2019a).
- In the $M_{\text{BH}}-R_{\text{e,sph}}$ diagram, ETGs with a disk (ES, S0) and ETGs without a disk (E) follow two different, almost parallel, relations with slopes $\sim 2 \pm 0.2$ (Figure 12), which are steeper than the above single-regression $M_{\text{BH}}-R_{\text{e,sph}}$ relation for all ETGs (see Tables 1 and 2 for parameters) and offset by a factor of ~ 10 in the vertical M_{BH} -direction. This is again analogous to the offset observed between the $M_{\text{BH}}-M_{*,\text{sph}}$ relations followed by ETGs with and without a disk (Sahu et al. 2019a). Given $M_{*,\text{sph}}$ depends on $R_{\text{e,sph}}$ via $M_{*,\text{sph}} = (M/L)2\pi R_{\text{e}}^2 \langle I \rangle_{\text{e}}$, we find that the offset in the $M_{\text{BH}}-M_{*,\text{sph}}$ diagram originates from the offset between ETGs with and without a disk in the $M_{\text{BH}}-R_{\text{e,sph}}$ diagram. The reason behind the offset is the smaller spheroid half-light radius of ETGs with a disk relative to that of elliptical (purely spheroidal) galaxies.
- In the $M_{*,\text{sph}}-R_{\text{z,sph}}$ and $M_{\text{BH}}-R_{\text{z,sph}}$ diagrams for $z=10\%$ and 90% (see Figures 10 and 14), we recover the same substructures as the $M_{\text{BH}}-R_{\text{e,sph}}$ and $M_{*,\text{sph}}-R_{\text{e,sph}}$ relations mentioned above, with the slopes of correlations gradually decreasing with increasing z (see Table 2 for parameters).

The $M_{\text{BH}}-n_{\text{sph}}$ and $M_{\text{BH}}-R_{\text{e,sph}}$ relations may be useful for predicting the black hole masses of galaxies us-

ing their bulge Sérsic index or bulge half-light radius parameters. These parameters can be obtained by performing a multi-component decomposition of a galaxy light profile obtained even from a photometrically uncalibrated image. One should be careful while using the $M_{\text{BH}}-R_{\text{e,sph}}$ relation, because ETGs with a disk (ES,S0), ETGs without a disk (E), and LTGs (spirals) are found to follow different trends (Figures 11 and 12). However, when extended ETG or LTG classification is not known, the single regression $M_{\text{BH}}-n_{\text{sph}}$ or $M_{\text{BH}}-R_{\text{e,sph}}$ relations (provided in Tables 1 and 2) can still be used to predict M_{BH} , albeit with a higher uncertainty.

Our BH scaling relations, based on local galaxies, form a benchmark for studies investigating the evolution of BH correlations with galaxy properties across cosmic time (Lapi et al. 2014; Park et al. 2015; Sexton et al. 2019; Suh et al. 2020). In addition to enabling one to determine the black hole mass function (e.g. McLure & Dunlop 2004; Shankar et al. 2004; Graham et al. 2007; Vika et al. 2009; Davis et al. 2014; Mutlu-Pakdil et al. 2016), these BH scaling relations with bulge Sérsic parameters can also be employed to infer the lifetime of binary black holes (Biava et al. 2019; Li et al. 2020a) and further constrain the BH merger rate. The creation of merger-built spheroids with (initially) higher central stellar densities — which are associated with higher Sérsic indices — should, through dynamical friction (e.g., Chandrasekhar 1943; Arca-Sedda & Capuzzo-Dolcetta 2014), experience a quicker inspiral and hardening phase for their binary black holes. The imprint of such processes are the phase-space loss-cones (Begelman et al. 1980) observed as partially-depleted cores in massive spheroids (King & Minkowski 1966, 1972; Lauer 1985; Ferrarese et al. 1994; Trujillo et al. 2004; Dullo & Graham 2014). The eventual coalescence of the black holes results in the emission of gravitational waves (Poincaré 1906; Einstein 1916, 1918; Abbott et al. 2016). Our BH scaling relations will play a key role in constraining the detection of low-frequency gravitational waves generated from BH mergers at high redshifts, which fall in the detection domain of pulsar timing arrays (Shannon et al. 2015; Lentati et al. 2015; Sesana et al. 2016; Arzoumanian et al. 2018) and LISA (Amaro-Seoane et al. 2017; Barack et al. 2019).

The different scaling relations for ETGs and LTGs also hold valuable information for simulations, analytical/semi-analytical, and theoretical models of galaxy formation and evolution (e.g. Volonteri & Ciotti 2013; Heckman & Best 2014; Conselice 2014), as they reveal the trends of BH—host bulge/galaxy properties depending on galaxy morphology. These relations can be used for primary size and structure tests in simulations

aiming to generate realistic galaxies with supermassive black holes at their center (e.g. Schaye et al. 2015; Hopkins et al. 2018; Mutlu-Pakdil et al. 2018; Davé et al. 2019; Li et al. 2020b). We plan to test our new constraints through a comparison with simulations in our future work. Using our extensive dataset, we will present the correlation of black hole mass with the internal stellar density of galactic spheroids (N. Sahu et al. 2021, in preparation). We will also explore the (first morphology aware) fundamental plane in our future work.

ACKNOWLEDGMENTS

We thank the anonymous referee whose comments helped us improve the clarity of this paper. This research was conducted with the Australian Research Council Centre of Excellence for Gravitational Wave Discovery (OzGrav), through project number CE170100004. This project was supported under the Australian Research Council’s funding scheme DP17012923. This work has made use of the NASA/IPAC Infrared Science Archive, the NASA/IPAC Extragalactic Database (NED), and the HYPERLEDA Database <http://leda.univ-lyon1.fr/>.

REFERENCES

- Abbott, B. P., Abbott, R., Abbott, T. D., et al. 2016, *PhRvL*, 116, 061102, doi: [10.1103/PhysRevLett.116.061102](https://doi.org/10.1103/PhysRevLett.116.061102)
- Akritas, M. G., & Bershadsky, M. A. 1996, *ApJ*, 470, 706, doi: [10.1086/177901](https://doi.org/10.1086/177901)
- Amaro-Seoane, P., Audley, H., Babak, S., et al. 2017, arXiv e-prints, arXiv:1702.00786. <https://arxiv.org/abs/1702.00786>
- Andredakis, Y. C., Peletier, R. F., & Balcells, M. 1995, *MNRAS*, 275, 874, doi: [10.1093/mnras/275.3.874](https://doi.org/10.1093/mnras/275.3.874)
- Arca-Sedda, M., & Capuzzo-Dolcetta, R. 2014, *ApJ*, 785, 51, doi: [10.1088/0004-637X/785/1/51](https://doi.org/10.1088/0004-637X/785/1/51)
- Arzoumanian, Z., Baker, P. T., Brazier, A., et al. 2018, *ApJ*, 859, 47, doi: [10.3847/1538-4357/aabd3b](https://doi.org/10.3847/1538-4357/aabd3b)
- Athanassoula, E., Laurikainen, E., Salo, H., & Bosma, A. 2015, *MNRAS*, 454, 3843, doi: [10.1093/mnras/stv2231](https://doi.org/10.1093/mnras/stv2231)
- Baes, M., Buyle, P., Hau, G. K. T., & Dejonghe, H. 2003, *MNRAS*, 341, L44, doi: [10.1046/j.1365-8711.2003.06680.x](https://doi.org/10.1046/j.1365-8711.2003.06680.x)
- Baker, J., Barke, S. F., Bender, P. L., et al. 2019, arXiv e-prints, arXiv:1907.11305. <https://arxiv.org/abs/1907.11305>
- Barack, L., Cardoso, V., Nissanke, S., et al. 2019, *Classical and Quantum Gravity*, 36, 143001, doi: [10.1088/1361-6382/ab0587](https://doi.org/10.1088/1361-6382/ab0587)
- Batcheldor, D., Robinson, A., Axon, D. J., Perlman, E. S., & Merritt, D. 2010, *ApJ*, 717, L6, doi: [10.1088/2041-8205/717/1/L6](https://doi.org/10.1088/2041-8205/717/1/L6)
- Begelman, M. C. 1984, in *IAU Symposium*, Vol. 110, VLBI and Compact Radio Sources, ed. R. Fanti, K. I. Kellermann, & G. Setti, 227
- Begelman, M. C., Blandford, R. D., & Rees, M. J. 1980, *Nature*, 287, 307, doi: [10.1038/287307a0](https://doi.org/10.1038/287307a0)
- Beifiori, A., Courteau, S., Corsini, E. M., & Zhu, Y. 2012, *MNRAS*, 419, 2497, doi: [10.1111/j.1365-2966.2011.19903.x](https://doi.org/10.1111/j.1365-2966.2011.19903.x)
- Berrier, J. C., Davis, B. L., Kenefick, D., et al. 2013, *ApJ*, 769, 132, doi: [10.1088/0004-637X/769/2/132](https://doi.org/10.1088/0004-637X/769/2/132)
- Biava, N., Colpi, M., Capelo, P. R., et al. 2019, *MNRAS*, 487, 4985, doi: [10.1093/mnras/stz1614](https://doi.org/10.1093/mnras/stz1614)
- Blom, C., Forbes, D. A., Foster, C., Romanowsky, A. J., & Brodie, J. P. 2014, *MNRAS*, 439, 2420, doi: [10.1093/mnras/stu095](https://doi.org/10.1093/mnras/stu095)
- Bogdán, Á., Lovisari, L., Volonteri, M., & Dubois, Y. 2018, *ApJ*, 852, 131, doi: [10.3847/1538-4357/aa9ab5](https://doi.org/10.3847/1538-4357/aa9ab5)
- Caon, N., Capaccioli, M., & D’Onofrio, M. 1993a, *MNRAS*, 265, 1013, doi: [10.1093/mnras/265.4.1013](https://doi.org/10.1093/mnras/265.4.1013)

- . 1993b, MNRAS, 265, 1013, doi: [10.1093/mnras/265.4.1013](https://doi.org/10.1093/mnras/265.4.1013)
- Capaccioli, M. 1989, in *World of Galaxies (Le Monde des Galaxies)*, ed. J. Corwin, Harold G. & L. Bottinelli, 208–227
- Casura, S., Liske, J., Robotham, A. S. G., Taranu, D. S., & Laine, J. 2019, in *The Art of Measuring Galaxy Physical Properties*, 26, doi: [10.5281/zenodo.3556629](https://doi.org/10.5281/zenodo.3556629)
- Chandrasekhar, S. 1943, ApJ, 97, 255, doi: [10.1086/144517](https://doi.org/10.1086/144517)
- Chen, S., Sesana, A., & Conselice, C. J. 2019, MNRAS, 488, 401, doi: [10.1093/mnras/stz1722](https://doi.org/10.1093/mnras/stz1722)
- Choi, E., Somerville, R. S., Ostriker, J. P., Naab, T., & Hirschmann, M. 2018, ApJ, 866, 91, doi: [10.3847/1538-4357/aae076](https://doi.org/10.3847/1538-4357/aae076)
- Ciambur, B. C. 2015, ApJ, 810, 120, doi: [10.1088/0004-637X/810/2/120](https://doi.org/10.1088/0004-637X/810/2/120)
- . 2016, PASA, 33, e062, doi: [10.1017/pasa.2016.60](https://doi.org/10.1017/pasa.2016.60)
- Ciambur, B. C., Fragkoudi, F., Khoperskov, S., Di Matteo, P., & Combes, F. 2020, arXiv e-prints, arXiv:2003.00015. <https://arxiv.org/abs/2003.00015>
- Ciambur, B. C., & Graham, A. W. 2016, MNRAS, 459, 1276, doi: [10.1093/mnras/stw759](https://doi.org/10.1093/mnras/stw759)
- Combes, F., Debbasch, F., Friedli, D., & Pfenniger, D. 1990, A&A, 233, 82
- Conselice, C. J. 2014, ARA&A, 52, 291, doi: [10.1146/annurev-astro-081913-040037](https://doi.org/10.1146/annurev-astro-081913-040037)
- Danzmann, K. 2017, in *Society of Photo-Optical Instrumentation Engineers (SPIE) Conference Series*, Vol. 10566, Proc. SPIE, 1056610, doi: [10.1117/12.2308272](https://doi.org/10.1117/12.2308272)
- Davé, R., Anglés-Alcázar, D., Narayanan, D., et al. 2019, MNRAS, 486, 2827, doi: [10.1093/mnras/stz937](https://doi.org/10.1093/mnras/stz937)
- Davis, B. L., Graham, A. W., & Cameron, E. 2018, ApJ, 869, 113, doi: [10.3847/1538-4357/aae820](https://doi.org/10.3847/1538-4357/aae820)
- Davis, B. L., Graham, A. W., & Cameron, E. 2019, ApJ, 873, 85, doi: [10.3847/1538-4357/aaf3b8](https://doi.org/10.3847/1538-4357/aaf3b8)
- Davis, B. L., Graham, A. W., & Combes, F. 2019, ApJ, 877, 64, doi: [10.3847/1538-4357/ab1aa4](https://doi.org/10.3847/1538-4357/ab1aa4)
- Davis, B. L., Graham, A. W., & Seigar, M. S. 2017, MNRAS, 471, 2187, doi: [10.1093/mnras/stx1794](https://doi.org/10.1093/mnras/stx1794)
- Davis, B. L., Berrier, J. C., Johns, L., et al. 2014, ApJ, 789, 124, doi: [10.1088/0004-637X/789/2/124](https://doi.org/10.1088/0004-637X/789/2/124)
- de Nicola, S., Marconi, A., & Longo, G. 2019, MNRAS, 2130, doi: [10.1093/mnras/stz2472](https://doi.org/10.1093/mnras/stz2472)
- den Brok, M., Seth, A. C., Barth, A. J., et al. 2015, ApJ, 809, 101, doi: [10.1088/0004-637X/809/1/101](https://doi.org/10.1088/0004-637X/809/1/101)
- Dolag, K. 2015, in *IAU General Assembly*, Vol. 29, 2250156
- Dressler, A. 1989, in *Active Galactic Nuclei*, Vol. 134, 217
- Dullo, B. T., Bouquin, A. Y. K., Gil De Paz, A., Knapen, J. H., & Gorgas, J. 2020, arXiv e-prints, arXiv:2006.10128. <https://arxiv.org/abs/2006.10128>
- Dullo, B. T., & Graham, A. W. 2014, MNRAS, 444, 2700, doi: [10.1093/mnras/stu1590](https://doi.org/10.1093/mnras/stu1590)
- Einstein, A. 1916, *Sitzungsberichte der Königlich Preußischen Akademie der Wissenschaften (Berlin)*, 688
- . 1918, *Sitzungsberichte der Königlich Preußischen Akademie der Wissenschaften (Berlin)*, 154
- Ferrarese, L. 2002, ApJ, 578, 90, doi: [10.1086/342308](https://doi.org/10.1086/342308)
- Ferrarese, L., & Merritt, D. 2000, ApJ, 539, L9, doi: [10.1086/312838](https://doi.org/10.1086/312838)
- Ferrarese, L., van den Bosch, F. C., Ford, H. C., Jaffe, W., & O’Connell, R. W. 1994, AJ, 108, 1598, doi: [10.1086/117180](https://doi.org/10.1086/117180)
- Ferrarese, L., Côté, P., Jordán, A., et al. 2006, ApJS, 164, 334, doi: [10.1086/501350](https://doi.org/10.1086/501350)
- Fisher, D. B., & Drory, N. 2010, ApJ, 716, 942, doi: [10.1088/0004-637X/716/2/942](https://doi.org/10.1088/0004-637X/716/2/942)
- Fisher, D. B., & Drory, N. 2016, in *Astrophysics and Space Science Library*, Vol. 418, Galactic Bulges, ed. E. Laurikainen, R. Peletier, & D. Gadotti, 41, doi: [10.1007/978-3-319-19378-6_3](https://doi.org/10.1007/978-3-319-19378-6_3)
- Fukugita, M., & Peebles, P. J. E. 2004, ApJ, 616, 643, doi: [10.1086/425155](https://doi.org/10.1086/425155)
- Gebhardt, K., Bender, R., Bower, G., et al. 2000, ApJ, 539, L13, doi: [10.1086/312840](https://doi.org/10.1086/312840)
- Graham, A., Lauer, T. R., Colless, M., & Postman, M. 1996, ApJ, 465, 534, doi: [10.1086/177440](https://doi.org/10.1086/177440)
- Graham, A. W. 2001, AJ, 121, 820, doi: [10.1086/318767](https://doi.org/10.1086/318767)
- . 2012, ApJ, 746, 113, doi: [10.1088/0004-637X/746/1/113](https://doi.org/10.1088/0004-637X/746/1/113)
- Graham, A. W. 2016, in *Astrophysics and Space Science Library*, Vol. 418, Galactic Bulges, ed. E. Laurikainen, R. Peletier, & D. Gadotti, 263, doi: [10.1007/978-3-319-19378-6_11](https://doi.org/10.1007/978-3-319-19378-6_11)
- . 2019a, MNRAS, 1547, doi: [10.1093/mnras/stz1623](https://doi.org/10.1093/mnras/stz1623)
- . 2019b, PASA, 36, e035, doi: [10.1017/pasa.2019.23](https://doi.org/10.1017/pasa.2019.23)
- Graham, A. W., Ciambur, B. C., & Savorgnan, G. A. D. 2016a, ApJ, 831, 132, doi: [10.3847/0004-637X/831/2/132](https://doi.org/10.3847/0004-637X/831/2/132)
- Graham, A. W., & Driver, S. P. 2005, *Publications of the Astronomical Society of Australia*, 22, 118, doi: [10.1071/AS05001](https://doi.org/10.1071/AS05001)
- . 2007a, ApJ, 655, 77, doi: [10.1086/509758](https://doi.org/10.1086/509758)
- . 2007b, MNRAS, 380, L15, doi: [10.1111/j.1745-3933.2007.00340.x](https://doi.org/10.1111/j.1745-3933.2007.00340.x)
- Graham, A. W., Durré, M., Savorgnan, G. A. D., et al. 2016b, ApJ, 819, 43, doi: [10.3847/0004-637X/819/1/43](https://doi.org/10.3847/0004-637X/819/1/43)
- Graham, A. W., Erwin, P., Caon, N., & Trujillo, I. 2001a, ApJL, 563, L11, doi: [10.1086/338500](https://doi.org/10.1086/338500)

- Graham, A. W., Erwin, P., Caon, N., & Trujillo, I. 2003a, in *Revista Mexicana de Astronomia y Astrofisica Conference Series*, Vol. 17, *Revista Mexicana de Astronomia y Astrofisica Conference Series*, ed. V. Avila-Reese, C. Firmani, C. S. Frenk, & C. Allen, 196–197. <https://arxiv.org/abs/astro-ph/0206248>
- Graham, A. W., & Guzmán, R. 2003, *AJ*, 125, 2936, doi: [10.1086/374992](https://doi.org/10.1086/374992)
- Graham, A. W., Merritt, D., Moore, B., Diemand, J., & Terzić, B. 2006, *AJ*, 132, 2711, doi: [10.1086/508992](https://doi.org/10.1086/508992)
- Graham, A. W., & Scott, N. 2013, *ApJ*, 764, 151, doi: [10.1088/0004-637X/764/2/151](https://doi.org/10.1088/0004-637X/764/2/151)
- Graham, A. W., Trujillo, I., & Caon, N. 2001b, *AJ*, 122, 1707, doi: [10.1086/323090](https://doi.org/10.1086/323090)
- Graham, A. W., & Worley, C. C. 2008, *MNRAS*, 388, 1708, doi: [10.1111/j.1365-2966.2008.13506.x](https://doi.org/10.1111/j.1365-2966.2008.13506.x)
- Graham, A. W., et al. 2003b, *AJ*, 125, 2951, doi: [10.1086/375320](https://doi.org/10.1086/375320)
- . 2007, *MNRAS*, 378, 198, doi: [10.1111/j.1365-2966.2007.11770.x](https://doi.org/10.1111/j.1365-2966.2007.11770.x)
- Häußler, B., Bamford, S. P., Vika, M., et al. 2013, *MNRAS*, 430, 330, doi: [10.1093/mnras/sts633](https://doi.org/10.1093/mnras/sts633)
- Heckman, T. M., & Best, P. N. 2014, *ARA&A*, 52, 589, doi: [10.1146/annurev-astro-081913-035722](https://doi.org/10.1146/annurev-astro-081913-035722)
- Hopkins, P. F., Wetzell, A., Kereš, D., et al. 2018, *MNRAS*, 480, 800, doi: [10.1093/mnras/sty1690](https://doi.org/10.1093/mnras/sty1690)
- Jerjen, H., Binggeli, B., & Freeman, K. C. 2000, *AJ*, 119, 593, doi: [10.1086/301216](https://doi.org/10.1086/301216)
- Kelly, B. C., & Merloni, A. 2012, *Advances in Astronomy*, 2012, 970858, doi: [10.1155/2012/970858](https://doi.org/10.1155/2012/970858)
- Kelvin, L. S., Driver, S. P., Robotham, A. S. G., et al. 2012, *MNRAS*, 421, 1007, doi: [10.1111/j.1365-2966.2012.20355.x](https://doi.org/10.1111/j.1365-2966.2012.20355.x)
- Kennedy, R., Bamford, S. P., Häußler, B., et al. 2016, *MNRAS*, 460, 3458, doi: [10.1093/mnras/stw1176](https://doi.org/10.1093/mnras/stw1176)
- Kent, S. M., Dame, T. M., & Fazio, G. 1991, *ApJ*, 378, 131, doi: [10.1086/170413](https://doi.org/10.1086/170413)
- Khosroshahi, H. G., Wadadekar, Y., & Kembhavi, A. 2000, *ApJ*, 533, 162, doi: [10.1086/308654](https://doi.org/10.1086/308654)
- King, I. R., & Minkowski, R. 1966, *ApJ*, 143, 1002, doi: [10.1086/148580](https://doi.org/10.1086/148580)
- King, I. R., & Minkowski, R. 1972, in *IAU Symposium*, Vol. 44, *External Galaxies and Quasi-Stellar Objects*, ed. D. S. Evans, D. Wills, & B. J. Wills, 87
- Klypin, A. A., Trujillo-Gomez, S., & Primack, J. 2011, *ApJ*, 740, 102, doi: [10.1088/0004-637X/740/2/102](https://doi.org/10.1088/0004-637X/740/2/102)
- Kormendy, J., & Bender, R. 2012, *ApJS*, 198, 2, doi: [10.1088/0067-0049/198/1/2](https://doi.org/10.1088/0067-0049/198/1/2)
- Kormendy, J., Fisher, D. B., Cornell, M. E., & Bender, R. 2009, *ApJS*, 182, 216, doi: [10.1088/0067-0049/182/1/216](https://doi.org/10.1088/0067-0049/182/1/216)
- Kormendy, J., & Richstone, D. 1995, *ARA&A*, 33, 581, doi: [10.1146/annurev.aa.33.090195.003053](https://doi.org/10.1146/annurev.aa.33.090195.003053)
- Lange, R., Driver, S. P., Robotham, A. S. G., et al. 2015, *MNRAS*, 447, 2603, doi: [10.1093/mnras/stu2467](https://doi.org/10.1093/mnras/stu2467)
- Laor, A. 2001, *ApJ*, 553, 677, doi: [10.1086/320989](https://doi.org/10.1086/320989)
- Lapi, A., Raimundo, S., Aversa, R., et al. 2014, *ApJ*, 782, 69, doi: [10.1088/0004-637X/782/2/69](https://doi.org/10.1088/0004-637X/782/2/69)
- Lauer, T. R. 1985, *ApJ*, 292, 104, doi: [10.1086/163136](https://doi.org/10.1086/163136)
- Laurikainen, E., Salo, H., Buta, R., Knapen, J. H., & Comerón, S. 2010, *MNRAS*, 405, 1089, doi: [10.1111/j.1365-2966.2010.16521.x](https://doi.org/10.1111/j.1365-2966.2010.16521.x)
- Lentati, L., Taylor, S. R., Mingarelli, C. M. F., et al. 2015, *MNRAS*, 453, 2576, doi: [10.1093/mnras/stv1538](https://doi.org/10.1093/mnras/stv1538)
- Li, K., Bogdanovic, T., & Ballantyne, D. R. 2020a, *arXiv e-prints*, arXiv:2007.02051. <https://arxiv.org/abs/2007.02051>
- Li, Y., Habouzit, M., Genel, S., et al. 2020b, *ApJ*, 895, 102, doi: [10.3847/1538-4357/ab8f8d](https://doi.org/10.3847/1538-4357/ab8f8d)
- Licquia, T. C., & Newman, J. A. 2015, *ApJ*, 806, 96, doi: [10.1088/0004-637X/806/1/96](https://doi.org/10.1088/0004-637X/806/1/96)
- Liller, M. H. 1966, *ApJ*, 146, 28, doi: [10.1086/148857](https://doi.org/10.1086/148857)
- Magorrian, J., Tremaine, S., Richstone, D., et al. 1998, *AJ*, 115, 2285, doi: [10.1086/300353](https://doi.org/10.1086/300353)
- Markwardt, C. 2012, *MPFIT: Robust non-linear least squares curve fitting*. <http://ascl.net/1208.019>
- Marshall, M. A., Mutch, S. J., Qin, Y., Poole, G. B., & Wyithe, J. S. B. 2020, *MNRAS*, 494, 2747, doi: [10.1093/mnras/staa936](https://doi.org/10.1093/mnras/staa936)
- Martín-Navarro, I., Burchett, J. N., & Mezcuca, M. 2020, *MNRAS*, 491, 1311, doi: [10.1093/mnras/stz3073](https://doi.org/10.1093/mnras/stz3073)
- McLure, R. J., & Dunlop, J. S. 2004, *MNRAS*, 352, 1390, doi: [10.1111/j.1365-2966.2004.08034.x](https://doi.org/10.1111/j.1365-2966.2004.08034.x)
- Möllenhoff, C., & Heidt, J. 2001, *A&A*, 368, 16, doi: [10.1051/0004-6361:20000335](https://doi.org/10.1051/0004-6361:20000335)
- Mutlu-Pakdil, B., Seigar, M. S., & Davis, B. L. 2016, *ApJ*, 830, 117, doi: [10.3847/0004-637X/830/2/117](https://doi.org/10.3847/0004-637X/830/2/117)
- Mutlu-Pakdil, B., Seigar, M. S., Hewitt, I. B., et al. 2018, *MNRAS*, 474, 2594, doi: [10.1093/mnras/stx2935](https://doi.org/10.1093/mnras/stx2935)
- Nemmen, R. S., Georganopoulos, M., Guiriec, S., et al. 2012, *Science*, 338, 1445, doi: [10.1126/science.1227416](https://doi.org/10.1126/science.1227416)
- Novak, G. S., Faber, S. M., & Dekel, A. 2006, *ApJ*, 637, 96, doi: [10.1086/498333](https://doi.org/10.1086/498333)
- Park, D., Woo, J.-H., Bennert, V. N., et al. 2015, *ApJ*, 799, 164, doi: [10.1088/0004-637X/799/2/164](https://doi.org/10.1088/0004-637X/799/2/164)
- Paturel, G., Petit, C., Prugniel, P., et al. 2003, *A&A*, 412, 45, doi: [10.1051/0004-6361:20031411](https://doi.org/10.1051/0004-6361:20031411)
- Pillepich, A., Springel, V., Nelson, D., et al. 2018, *MNRAS*, 473, 4077, doi: [10.1093/mnras/stx2656](https://doi.org/10.1093/mnras/stx2656)

- Planck Collaboration, Aghanim, N., Akrami, Y., et al. 2018, ArXiv e-prints, arXiv:1807.06209. <https://arxiv.org/abs/1807.06209>
- Poincaré, H. 1906, Academie des Sciences Paris Comptes Rendus, 150, 1504
- Press, W. H., Teukolsky, S. A., Vetterling, W. T., & Flannery, B. P. 1992, Numerical recipes in FORTRAN. The art of scientific computing
- Querejeta, M., Meidt, S. E., Schinnerer, E., et al. 2015, The Astrophysical Journal Supplement Series, 219, 5, doi: [10.1088/0067-0049/219/1/5](https://doi.org/10.1088/0067-0049/219/1/5)
- Ruszkowski, M., Nagai, D., Zhuravleva, I., et al. 2019, BAAS, 51, 326. <https://arxiv.org/abs/1903.09686>
- Sahu, N., Graham, A. W., & Davis, B. L. 2019a, ApJ, 876, 155, doi: [10.3847/1538-4357/ab0f32](https://doi.org/10.3847/1538-4357/ab0f32)
- . 2019b, ApJ, 887, 10, doi: [10.3847/1538-4357/ab50b7](https://doi.org/10.3847/1538-4357/ab50b7)
- Salucci, P., et al. 2000, MNRAS, 317, 488, doi: [10.1046/j.1365-8711.2000.03622.x](https://doi.org/10.1046/j.1365-8711.2000.03622.x)
- Savorgnan, G., Graham, A. W., Marconi, A., et al. 2013, MNRAS, 434, 387, doi: [10.1093/mnras/stt1027](https://doi.org/10.1093/mnras/stt1027)
- Savorgnan, G. A. D. 2016, ApJ, 821, 88, doi: [10.3847/0004-637X/821/2/88](https://doi.org/10.3847/0004-637X/821/2/88)
- Savorgnan, G. A. D., & Graham, A. W. 2016, ApJS, 222, 10, doi: [10.3847/0067-0049/222/1/10](https://doi.org/10.3847/0067-0049/222/1/10)
- Savorgnan, G. A. D., et al. 2016, ApJ, 817, 21, doi: [10.3847/0004-637X/817/1/21](https://doi.org/10.3847/0004-637X/817/1/21)
- Schaye, J., Crain, R. A., Bower, R. G., et al. 2015, MNRAS, 446, 521, doi: [10.1093/mnras/stu2058](https://doi.org/10.1093/mnras/stu2058)
- Scott, N., Graham, A. W., & Schombert, J. 2013, ApJ, 768, 76, doi: [10.1088/0004-637X/768/1/76](https://doi.org/10.1088/0004-637X/768/1/76)
- Secrest, N. J., Satyapal, S., Moran, S. M., et al. 2013, ApJ, 777, 139, doi: [10.1088/0004-637X/777/2/139](https://doi.org/10.1088/0004-637X/777/2/139)
- Seigar, M. S., Kenefick, D., Kenefick, J., & Lacy, C. H. S. 2008, ApJL, 678, L93, doi: [10.1086/588727](https://doi.org/10.1086/588727)
- Sérsic, J. L. 1963, BAAA, 6, 41
- . 1968a, Atlas de Galaxies Australes - English Translation of the chapter “Photometric Analysis”, Tech. rep., doi: [10.5281/zenodo.2562394](https://doi.org/10.5281/zenodo.2562394)
- . 1968b, Bulletin of the Astronomical Institutes of Czechoslovakia, 19, 105
- Sesana, A., Shankar, F., Bernardi, M., & Sheth, R. K. 2016, MNRAS, 463, L6, doi: [10.1093/mnras/slw139](https://doi.org/10.1093/mnras/slw139)
- Sexton, R. O., Canalizo, G., Hiner, K. D., et al. 2019, ApJ, 878, 101, doi: [10.3847/1538-4357/ab21d5](https://doi.org/10.3847/1538-4357/ab21d5)
- Shankar, F., Salucci, P., Granato, G. L., De Zotti, G., & Danese, L. 2004, MNRAS, 354, 1020, doi: [10.1111/j.1365-2966.2004.08261.x](https://doi.org/10.1111/j.1365-2966.2004.08261.x)
- Shannon, R. M., Ravi, V., Lentati, L. T., et al. 2015, Science, 349, 1522, doi: [10.1126/science.aab1910](https://doi.org/10.1126/science.aab1910)
- Siemens, X., Ellis, J., Jenet, F., & Romano, J. D. 2013, Classical and Quantum Gravity, 30, 224015, doi: [10.1088/0264-9381/30/22/224015](https://doi.org/10.1088/0264-9381/30/22/224015)
- Simmons, B. D., Lintott, C., Schawinski, K., et al. 2013, MNRAS, 429, 2199, doi: [10.1093/mnras/sts491](https://doi.org/10.1093/mnras/sts491)
- Somerville, R. S., & Davé, R. 2015, ARA&A, 53, 51, doi: [10.1146/annurev-astro-082812-140951](https://doi.org/10.1146/annurev-astro-082812-140951)
- Suh, H., Civano, F., Trakhtenbrot, B., et al. 2020, ApJ, 889, 32, doi: [10.3847/1538-4357/ab5f5f](https://doi.org/10.3847/1538-4357/ab5f5f)
- Terrazas, B. A., Bell, E. F., Henriques, B. M. B., et al. 2016, ApJL, 830, L12, doi: [10.3847/2041-8205/830/1/L12](https://doi.org/10.3847/2041-8205/830/1/L12)
- Terrazas, B. A., Bell, E. F., Pillepich, A., et al. 2020, MNRAS, 493, 1888, doi: [10.1093/mnras/staa374](https://doi.org/10.1093/mnras/staa374)
- Terzić, B., & Graham, A. W. 2005, MNRAS, 362, 197, doi: [10.1111/j.1365-2966.2005.09269.x](https://doi.org/10.1111/j.1365-2966.2005.09269.x)
- Tolstoy, E., Hill, V., & Tosi, M. 2009, ARA&A, 47, 371, doi: [10.1146/annurev-astro-082708-101650](https://doi.org/10.1146/annurev-astro-082708-101650)
- Tremaine, S., Gebhardt, K., Bender, R., et al. 2002, ApJ, 574, 740, doi: [10.1086/341002](https://doi.org/10.1086/341002)
- Trujillo, I., Erwin, P., Asensio Ramos, A., & Graham, A. W. 2004, AJ, 127, 1917, doi: [10.1086/382712](https://doi.org/10.1086/382712)
- Trujillo, I., Graham, A. W., & Caon, N. 2001, MNRAS, 326, 869, doi: [10.1046/j.1365-8711.2001.04471.x](https://doi.org/10.1046/j.1365-8711.2001.04471.x)
- van den Bosch, R. C. E. 2016, ApJ, 831, 134, doi: [10.3847/0004-637X/831/2/134](https://doi.org/10.3847/0004-637X/831/2/134)
- Vika, M., Driver, S. P., Cameron, E., Kelvin, L., & Robotham, A. 2012, MNRAS, 419, 2264, doi: [10.1111/j.1365-2966.2011.19881.x](https://doi.org/10.1111/j.1365-2966.2011.19881.x)
- Vika, M., Driver, S. P., Graham, A. W., & Liske, J. 2009, MNRAS, 400, 1451, doi: [10.1111/j.1365-2966.2009.15544.x](https://doi.org/10.1111/j.1365-2966.2009.15544.x)
- Vogelsberger, M., Genel, S., Springel, V., et al. 2014, MNRAS, 444, 1518, doi: [10.1093/mnras/stu1536](https://doi.org/10.1093/mnras/stu1536)
- Volonteri, M., & Ciotti, L. 2013, ApJ, 768, 29, doi: [10.1088/0004-637X/768/1/29](https://doi.org/10.1088/0004-637X/768/1/29)
- Volonteri, M., Natarajan, P., & Gültekin, K. 2011, ApJ, 737, 50, doi: [10.1088/0004-637X/737/2/50](https://doi.org/10.1088/0004-637X/737/2/50)
- Volonteri, M., Pfister, H., Beckman, R. S., et al. 2020, arXiv e-prints, arXiv:2005.04902. <https://arxiv.org/abs/2005.04902>
- Wandel, A. 1999, ApJ, 519, L39, doi: [10.1086/312106](https://doi.org/10.1086/312106)
- Williams, M. J., Bureau, M., & Cappellari, M. 2010, MNRAS, 409, 1330, doi: [10.1111/j.1365-2966.2010.17406.x](https://doi.org/10.1111/j.1365-2966.2010.17406.x)
- Wright, E. L. 2006, PASP, 118, 1711, doi: [10.1086/510102](https://doi.org/10.1086/510102)
- Yepes, G., Martínez-Vaquero, L. A., Gottlöber, S., & Hoffman, Y. 2009, in American Institute of Physics Conference Series, Vol. 1178, American Institute of Physics Conference Series, ed. C. Balazs & F. Wang, 64–75, doi: [10.1063/1.3264558](https://doi.org/10.1063/1.3264558)

Young, C. K., & Currie, M. J. 1994, MNRAS, 268, L11,
doi: [10.1093/mnras/268.1.L11](https://doi.org/10.1093/mnras/268.1.L11)

APPENDIX

A. DATA SET

In Table A1, first 83 galaxies are ETGs, and the remaining are LTGs, where the galaxies with a depleted core are marked with superscript “a” on their names in the first column. The spheroid Sérsic model parameters (n , R_{e} , μ), morphology, and spheroid stellar masses are taken from our previous studies Savorgnan & Graham (2016), Sahu et al. (2019a), and Davis et al. (2019). For NGC 1271 and NGC 1277 these parameters are borrowed from Graham et al. (2016a) and Graham et al. (2016b), respectively. Spheroid parameters for the Milky Way are taken from Graham & Driver (2007a) who used the uncalibrated bulge surface brightness profile of Milky Way from Kent et al. (1991). The spheroid mass of Milky Way is taken from Licquia & Newman (2015).

Correlations of $M_{*,\text{sph}}$ and M_{BH} with the equivalent-axis bulge parameters obtained using symmetric MPFITEXY regression are presented in Table A2. These relations are consistent with the corresponding relations obtained using the (bisector) BCES regression presented in Table 2.

Table A1. Galaxy Sample

No.	Galaxy	Band	T_{λ} & $\mathcal{M}_{\odot, \lambda}$ ($\frac{M_{\odot}}{L_{\odot}}$) & mag	Type	n_{maj}	$R_{e,maj}$	$\mu_{e,maj}$	$\log(\frac{I_{e,maj}}{M_{\odot}/pc^2})$	n_{eq}	$R_{e,eq}$	$\mu_{e,eq}$	$\log(\frac{I_{e,eq}}{M_{\odot}/pc^2})$	C	scale	$\log(\frac{M_{*,sph}}{M_{\odot}})$	Distance	$\log(\frac{M_{BH}}{M_{\odot}})$	Ref.
(1)	(2)	(3)	(4)	(5)	(6)	(7)	(8)	(9)	(10)	(11)	(12)	(13)	(14)	(15)	(16)	(17)	(18)	
				arcsec	$\frac{mag}{arcsec^2}$	dex	arcsec	$\frac{mag}{arcsec^2}$	arcsec	$\frac{mag}{arcsec^2}$	dex	$\frac{kpc}{arcsec}$	dex	Mpc	dex			
1	IC 1459 ^a	3.6 μ m	(0.6, 3.26)	E	6.60	63.10	18.49	2.32	7.00	57.30	18.59	2.28	0.60	0.1366	11.55 \pm 0.12	28.4	9.38 \pm 0.20	SG16
2	NGC 0821	3.6 μ m	(0.6, 3.26)	E	5.30	36.50	18.40	2.36	6.10	18.90	17.83	2.58	0.62	0.1127	10.69 \pm 0.33	23.4	7.59 \pm 0.17	SG16
3	NGC 1023	3.6 μ m	(0.6, 3.26)	SB0	2.10	9.20	14.96	3.73	2.00	7.40	14.79	3.80	0.32	0.0536	10.21 \pm 0.12	11.1	7.62 \pm 0.05	SG16
4	NGC 1316	3.6 μ m	(0.6, 3.26)	SAB0*	2.00	21.50	15.55	3.50	1.80	15.90	15.43	3.54	0.30	0.0897	11.05 \pm 0.26	18.6	8.18 \pm 0.26	SG16
5	NGC 1332	3.6 μ m	(0.6, 3.26)	ES	5.10	34.70	17.44	2.74	3.70	18.00	16.47	3.13	0.35	0.1074	11.05 \pm 0.33	22.3	9.16 \pm 0.07	SG16
6	NGC 1399 ^a	3.6 μ m	(0.6, 3.26)	E	10.00	405.10	21.80	1.00	10.00	338.10	21.53	1.10	0.63	0.0935	11.66 \pm 0.12	19.4	8.67 \pm 0.06	SG16
7	NGC 2549	3.6 μ m	(0.6, 3.26)	SB0	2.30	6.10	15.57	3.49	1.50	3.10	14.54	3.90	0.24	0.0594	9.59 \pm 0.12	12.3	7.15 \pm 0.6	SG16
8	NGC 2778	3.6 μ m	(0.6, 3.26)	SAB0	1.30	2.30	15.61	3.47	1.20	2.20	15.46	3.53	0.24	0.1074	9.41 \pm 0.26	22.3	7.18 \pm 0.34	SG16
9	NGC 3091 ^a	3.6 μ m	(0.6, 3.26)	E	7.60	100.50	20.43	1.55	6.60	51.20	19.47	1.94	0.49	0.2447	11.61 \pm 0.12	51.2	9.56 \pm 0.04	SG16
10	NGC 3115	3.6 μ m	(0.6, 3.26)	S0	4.40	43.60	16.67	3.04	5.10	34.40	16.85	2.97	0.58	0.0455	10.77 \pm 0.12	9.4	8.94 \pm 0.25	SG16
11	NGC 3245	3.6 μ m	(0.6, 3.26)	SAB0	2.90	4.40	14.96	3.73	1.70	2.40	14.00	4.12	0.24	0.0979	10.06 \pm 0.12	20.3	8.30 \pm 0.12	SG16
12	NGC 3377	3.6 μ m	(0.6, 3.26)	E	7.70	61.80	19.16	2.05	9.20	91.70	20.33	1.58	0.73	0.0527	10.48 \pm 0.26	10.9	7.89 \pm 0.04	SG16
13	NGC 3379 ^a	3.6 μ m	(0.6, 3.26)	E	5.20	57.20	17.93	2.54	5.30	50.90	17.84	2.58	0.53	0.0498	10.8 \pm 0.26	10.3	8.60 \pm 0.12	SG16
14	NGC 3384	3.6 μ m	(0.6, 3.26)	SAB0	1.60	5.50	14.21	4.03	1.80	5.60	14.56	3.89	0.32	0.0546	10.06 \pm 0.12	11.3	7.23 \pm 0.05	SG16
15	NGC 3414	3.6 μ m	(0.6, 3.26)	E	4.80	28.00	18.10	2.48	4.50	25.50	18.08	2.48	0.46	0.118	10.83 \pm 0.12	24.5	8.38 \pm 0.06	SG16
16	NGC 3489	3.6 μ m	(0.6, 3.26)	SB0	1.50	2.20	13.47	4.33	1.30	1.70	13.25	4.41	0.25	0.0565	9.54 \pm 0.26	11.7	6.76 \pm 0.07	SG16
17	NGC 3585	3.6 μ m	(0.6, 3.26)	E	5.20	105.00	19.13	2.06	6.30	86.30	19.24	2.02	0.65	0.094	11.3 \pm 0.26	19.5	8.49 \pm 0.13	SG16
18	NGC 3607	3.6 μ m	(0.6, 3.26)	E	5.50	69.30	19.00	2.12	5.60	65.50	19.01	2.11	0.54	0.107	11.23 \pm 0.26	22.2	8.11 \pm 0.18	SG16
19	NGC 3608 ^a	3.6 μ m	(0.6, 3.26)	E	5.20	47.50	18.93	2.14	5.70	43.40	19.00	2.12	0.58	0.1074	10.89 \pm 0.26	22.3	8.30 \pm 0.18	SG16
20	NGC 3842 ^a	3.6 μ m	(0.6, 3.26)	E	8.10	100.70	21.43	1.16	8.20	73.60	21.07	1.31	0.61	0.4643	11.92 \pm 0.12	98.4	9.99 \pm 0.13	SG16
21	NGC 3998	3.6 μ m	(0.6, 3.26)	SAB0	1.20	5.80	15.15	3.65	1.30	4.80	14.63	3.86	0.26	0.0662	10.02 \pm 0.33	13.7	8.91 \pm 0.11	SG16
22	NGC 4261 ^a	3.6 μ m	(0.6, 3.26)	E	4.70	52.60	18.58	2.29	4.30	47.30	18.53	2.31	0.45	0.1481	11.38 \pm 0.26	30.8	8.70 \pm 0.09	SG16
23	NGC 4291 ^a	3.6 μ m	(0.6, 3.26)	E	4.20	15.00	17.14	2.86	5.90	15.40	17.51	2.71	0.70	0.1228	10.71 \pm 0.26	25.5	8.52 \pm 0.36	SG16
24	NGC 4374 ^a	3.6 μ m	(0.6, 3.26)	E	7.80	101.60	19.01	2.11	7.90	129.8	19.57	1.89	0.60	0.0864	11.49 \pm 0.26	17.9	8.95 \pm 0.05	SG16
25	NGC 4459	3.6 μ m	(0.6, 3.26)	S0	3.10	18.40	16.69	3.04	2.60	13.00	16.23	3.22	0.34	0.0758	10.48 \pm 0.26	15.7	7.83 \pm 0.09	SG16
26	NGC 4472 ^a	3.6 μ m	(0.6, 3.26)	E	6.60	190.20	19.33	1.98	5.40	135.30	18.83	2.18	0.44	0.0825	11.7 \pm 0.12	17.1	9.40 \pm 0.05	SG16
27	NGC 4473	3.6 μ m	(0.6, 3.26)	E	2.30	45.90	17.93	2.54	2.90	36.90	18.10	2.47	0.46	0.0739	10.64 \pm 0.26	15.3	8.08 \pm 0.36	SG16
28	NGC 4486 ^a	3.6 μ m	(0.6, 3.26)	E	10.00	203.00	19.87	1.77	5.90	87.10	18.26	2.41	0.33	0.0753	11.49 \pm 0.26	16.8	9.81 \pm 0.05	SG16
29	NGC 4564	3.6 μ m	(0.6, 3.26)	S0	2.60	5.00	15.23	3.62	3.00	6.00	15.65	3.45	0.45	0.0705	10.01 \pm 0.12	14.6	7.78 \pm 0.06	SG16
30	NGC 4596	3.6 μ m	(0.6, 3.26)	SB0	2.70	6.60	15.93	3.34	3.00	9.00	16.44	3.14	0.44	0.082	10.18 \pm 0.12	17.0	7.90 \pm 0.20	SG16
31	NGC 4621	3.6 μ m	(0.6, 3.26)	E	5.50	48.00	18.02	2.51	8.80	90.90	19.67	1.85	0.87	0.0859	11.16 \pm 0.12	17.8	8.59 \pm 0.05	SG16
32	NGC 4697	3.6 μ m	(0.6, 3.26)	E	7.20	239.30	20.62	1.47	6.70	226.40	20.90	1.35	0.53	0.0551	11.01 \pm 0.33	11.4	8.26 \pm 0.05	SG16
33	NGC 4889 ^a	3.6 μ m	(0.6, 3.26)	E	8.10	119.70	21.01	1.33	6.80	60.80	20.11	1.69	0.48	0.4863	12.14 \pm 0.12	103.2	10.32 \pm 0.44	SG16
34	NGC 5077 ^a	3.6 μ m	(0.6, 3.26)	E	4.20	23.50	17.67	2.65	5.70	23.00	18.01	2.52	0.68	0.1975	11.28 \pm 0.12	41.2	8.87 \pm 0.22	SG16
35	NGC 5128	3.6 μ m	(0.6, 3.26)	S0*	1.20	61.30	15.73	3.42	2.20	60.80	16.01	3.30	0.42	0.0185	10.64 \pm 0.33	3.8	7.65 \pm 0.13	SG16

Table A1 continued

Table A1 (continued)

No.	Galaxy	Band	Υ_λ & $\mathcal{M}_{\odot,\lambda}$ ($\frac{M_\odot}{L_\odot}$) & mag	Type	n_{maj}	$R_{e,maj}$	$\mu_{e,maj}$	$\log(\frac{I_{e,maj}}{M_\odot/\text{pc}^2})$	n_{eq}	$R_{e,eq}$	$\mu_{e,eq}$	$\log(\frac{I_{e,eq}}{M_\odot/\text{pc}^2})$	C	scale	$\log(\frac{M_{*,sph}}{M_\odot})$	Distance	$\log(\frac{M_{PH}}{M_\odot})$	Ref.
(1)	(2)	(3)	(4)	(5)	(6)	(7)	(8)	(9)	(10)	(11)	(12)	(13)	(14)	(15)	(16)	(17)	(18)	
					arcsec	$\frac{\text{mag}}{\text{arcsec}^2}$	dex	arcsec	arcsec	$\frac{\text{mag}}{\text{arcsec}^2}$	dex	arcsec	$\frac{\text{kpc}}{\text{arcsec}}$	dex	Mpc	dex		
36	NGC 5576	3.6 μm	(0.6, 3.26)	E	3.30	61.50	19.41	1.95	3.70	49.30	19.34	1.98	0.49	0.1194	10.87 ± 0.12	24.8	8.20 ± 0.10	SG16
37	NGC 5846 ^a	3.6 μm	(0.6, 3.26)	E	6.40	105.10	19.67	1.85	5.70	83.40	19.28	2.01	0.48	0.1165	11.42 ± 0.26	24.2	9.04 ± 0.05	SG16
38	NGC 6251 ^a	3.6 μm	(0.6, 3.26)	E	6.80	41.70	19.82	1.81	5.60	30.10	19.31	2.01	0.44	0.4927	11.82 ± 0.12	104.6	8.77 ± 0.16	SG16
39	NGC 7619 ^a	3.6 μm	(0.6, 3.26)	E	5.30	63.20	19.53	1.91	5.20	58.00	19.55	1.90	0.51	0.2461	11.64 ± 0.26	51.5	9.40 ± 0.09	SG16
40	NGC 7768 ^a	3.6 μm	(0.6, 3.26)	E	8.40	92.90	21.37	1.19	6.70	42.10	20.15	1.68	0.45	0.5301	11.89 ± 0.26	112.8	9.11 ± 0.15	SG16
41	NGC 1271	H (HST)	(1.4, 3.33)	ES	4.26	3.25	16.75	3.43	4.16	3.07	16.79	3.41	0.46	0.3794	10.95 ± 0.1	80.0	9.48 ± 0.16	GCSI6a
42	NGC 1277	V (HST)	(11.65, 4.82)	ES	5.34	6.00	20.73	3.35	5.63	5.60	21.05	3.22	0.56	0.3445	11.43 ± 0.1	72.5	9.08 ± 0.12	GDS16b
43	A1836 BCG ^a	K _s	(0.7, 5.08)	E	4.10	23.99	19.36	2.80	3.47	14.75	20.66	2.28	0.39	0.7335	11.70 ± 0.12	158	9.59 ± 0.06	SGD19a
44	A3565 BCG	3.6 μm	(0.6, 6.02)	E	3.85	43.21	21.29	2.31	3.82	41.10	21.28	2.31	0.45	0.1951	11.47 ± 0.26	40.7	9.04 ± 0.09	SGD19a
45	NGC 0307	r (SDSS)	(2.8, 4.65)	SAB0	3.33	3.00	18.82	3.42	3.76	3.33	19.44	3.17	0.49	0.2523	10.43 ± 0.33	52.8	8.34 ± 0.13	SGD19a
46	NGC 0404	3.6 μm	(0.6, 6.02)	S0	0.93	3.99	18.58	3.39	0.90	3.89	18.59	3.38	0.20	0.0148	7.96 ± 0.27	3.1	4.85 ± 0.13	SGD19a
47	NGC 0524 ^a	3.6 μm	(0.6, 6.02)	SA0(rs)	2.29	8.79	18.67	3.35	2.16	8.35	18.57	3.39	0.34	0.1122	10.57 ± 0.26	23.3	8.92 ± 0.10	SGD19a
48	NGC 1194 ^a	3.6 μm	(0.6, 6.02)	S0*	3.76	3.52	18.34	3.49	3.91	3.56	18.56	3.40	0.47	0.2542	10.71 ± 0.33	53.2	7.81 ± 0.04	SGD19a
49	NGC 1275	3.6 μm	(0.6, 6.02)	E	4.78	70.69	22.62	1.78	4.31	53.6	22.27	1.92	0.44	0.3464	11.84 ± 0.26	72.9	8.90 ± 0.20	SGD19a
50	NGC 1374	3.6 μm	(0.6, 6.02)	S0	1.68	12.56	19.65	2.96	1.65	11.74	19.62	2.97	0.29	0.0926	10.22 ± 0.26	19.2	8.76 ± 0.05	SGD19a
51	NGC 1407 ^a	3.6 μm	(0.6, 6.02)	E	3.95	49.67	20.89	2.46	3.89	47.29	20.87	2.47	0.45	0.1349	11.46 ± 0.27	28	9.65 ± 0.08	SGD19a
52	NGC 1550 ^a	K _s	(0.7, 5.08)	E	7.50	24.80	20.87	2.17	7.48	24.8	21.16	2.05	0.58	0.2465	11.13 ± 0.12	51.6	9.57 ± 0.06	SGD19a
53	NGC 1600 ^a	3.6 μm	(0.6, 6.02)	E	7.14	76.57	22.66	1.77	5.08	49.58	21.98	2.04	0.38	0.3048	11.82 ± 0.12	64	10.23 ± 0.05	SGD19a
54	NGC 2787	3.6 μm	(0.6, 6.02)	SB0(r)	1.36	4.06	17.32	3.89	1.27	2.88	17.08	3.99	0.25	0.0353	9.13 ± 0.26	7.3	7.60 ± 0.06	SGD19a
55	NGC 3665	3.6 μm	(0.6, 6.02)	S0	2.76	14.44	19.28	3.11	2.74	12.78	19.34	3.09	0.39	0.1666	11.03 ± 0.26	34.7	8.76 ± 0.10	SGD19a
56	NGC 3923 ^a	3.6 μm	(0.6, 6.02)	E	4.78	85.97	21.50	2.22	4.77	78.78	21.55	2.20	0.5	0.1006	11.4 ± 0.15	20.9	9.45 ± 0.13	SGD19a
57	NGC 4026	3.6 μm	(0.6, 6.02)	SB0	3.45	3.10	16.14	4.36	3.98	2.35	16.04	4.40	0.51	0.0638	10.11 ± 0.33	13.2	8.26 ± 0.11	SGD19a
58	NGC 4339	3.6 μm	(0.6, 6.02)	S0	1.46	6.64	19.22	3.13	1.40	6.42	19.21	3.14	0.27	0.0772	9.67 ± 0.26	16.0	7.63 ± 0.33	SGD19a
59	NGC 4342	3.6 μm	(0.6, 6.02)	ES	3.48	4.22	18.48	3.43	3.99	4.69	19.23	3.13	0.51	0.1108	9.94 ± 0.25	23.0	8.65 ± 0.18	SGD19a
60	NGC 4350	3.6 μm	(0.6, 6.02)	EBS	4.30	18.84	20.8	2.50	3.97	19.45	20.75	2.52	0.44	0.0811	10.28 ± 0.26	16.8	8.86 ± 0.41	SGD19a
61	NGC 4371	3.6 μm	(0.6, 6.02)	SB(r)0	2.83	8.46	19.49	3.02	3.19	8.90	19.91	2.85	0.45	0.0816	9.89 ± 0.26	16.9	6.85 ± 0.08	SGD19a
62	NGC 4429	3.6 μm	(0.6, 6.02)	SB(r)0	2.56	16.42	19.05	3.20	2.31	11.29	18.78	3.31	0.34	0.0796	10.46 ± 0.26	16.5	8.18 ± 0.09	SGD19a
63	NGC 4434	3.6 μm	(0.6, 6.02)	S0	2.68	4.94	19.06	3.20	2.93	5.31	19.31	3.10	0.43	0.1079	9.91 ± 0.26	22.4	7.85 ± 0.17	SGD19a
64	NGC 4486B	r (SDSS)	(2.8, 4.65)	E	2.63	2.60	18.20	3.66	2.74	2.53	18.30	3.62	0.4	0.0739	9.47 ± 0.33	15.3	8.76 ± 0.24	SGD19a
65	NGC 4526	3.6 μm	(0.6, 6.02)	S0	2.28	13.01	18.19	3.54	2.96	14.88	18.98	3.23	0.47	0.0816	10.7 ± 0.26	16.9	8.67 ± 0.05	SGD19a
66	NGC 4552	3.6 μm	(0.6, 6.02)	E	5.42	83.62	22.12	1.97	5.36	71.5	21.92	2.05	0.52	0.0719	10.88 ± 0.25	14.9	8.67 ± 0.05	SGD19a
67	NGC 4578	3.6 μm	(0.6, 6.02)	S0(r)	2.30	7.82	19.26	3.11	1.99	6.32	19.14	3.16	0.31	0.0787	9.77 ± 0.26	16.3	7.28 ± 0.35	SGD19a
58	NGC 4649 ^a	3.6 μm	(0.6, 6.02)	E	4.96	93.03	21.01	2.42	5.21	80.59	20.98	2.43	0.54	0.0791	11.44 ± 0.12	16.4	9.67 ± 0.10	SGD19a
69	NGC 4742	3.6 μm	(0.6, 6.02)	S0	2.62	3.37	17.13	3.97	3.20	3.41	17.62	3.77	0.48	0.0748	9.87 ± 0.26	15.5	7.15 ± 0.18	SGD19a
70	NGC 4751 ^a	K _s	(0.7, 5.08)	S0	3.79	12.47	18.74	3.02	3.25	5.48	17.76	3.41	0.38	0.1295	10.49 ± 0.26	26.9	9.15 ± 0.05	SGD19a
71	NGC 4762	3.6 μm	(0.6, 6.02)	SB0	2.36	4.39	17.89	3.66	1.85	2.24	17.09	3.98	0.29	0.1089	9.97 ± 0.28	22.6	7.36 ± 0.15	SGD19a
72	NGC 5018	3.6 μm	(0.6, 6.02)	S0*	2.64	8.29	18.4	3.46	2.51	6.20	18.22	3.54	0.36	0.1944	10.98 ± 0.27	40.6	8.02 ± 0.09	SGD19a

Table A1 continued

Table A1 (continued)

No.	Galaxy	Band	Υ_λ & $\mathcal{M}_{\odot,\lambda}$ ($\frac{M_\odot}{L_\odot}$) & mag	Type	n_{maj}	$R_{e,maj}$	$\mu_{e,maj}$	$\log(\frac{I_{e,maj}}{M_\odot/pc^2})$	n_{eq}	$R_{e,eq}$	$\mu_{e,eq}$	$\log(\frac{I_{e,eq}}{M_\odot/pc^2})$	C	scale	$\log(\frac{M_{*,sph}}{M_\odot})$	Distance	$\log(\frac{M_{PH}}{M_\odot})$	Ref.
(1)	(2)	(3)	(4)	(5)	(6)	(7)	(8)	(9)	(10)	(11)	(12)	(13)	(14)	(15)	(16)	(17)	(18)	
73	NGC 5252	3.6 μ m	(0.6, 6.02)	S0	3.08	2.07	17.82	3.71	2.95	1.47	17.46	3.85	0.39	0.4569	10.85 \pm 0.26	96.8	9.00 \pm 0.40	SGD19a
74	NGC 5328 ^a	K _s	(0.7, 5.08)	E	6.58	25.11	20.29	2.40	5.21	22.46	20.26	2.42	0.42	0.3053	11.49 \pm 0.12	64.1	9.67 \pm 0.15	SGD19a
75	NGC 5419 ^a	3.6 μ m	(0.6, 6.02)	E	2.42	17.24	19.80	2.91	2.62	16.83	20.01	2.82	0.40	0.2683	11.45 \pm 0.12	56.2	9.86 \pm 0.14	SGD19a
76	NGC 5516 ^a	K _s	(0.7, 5.08)	E	5.99	51.27	21.54	1.90	5.32	32.30	20.86	2.18	0.47	0.2788	11.44 \pm 0.12	58.4	9.52 \pm 0.06	SGD19a
77	NGC 5813 ^a	3.6 μ m	(0.6, 6.02)	S0	4.02	18.54	20.74	2.53	3.65	14.16	19.81	2.90	0.42	0.1504	10.86 \pm 0.26	31.3	8.83 \pm 0.06	SGD19a
78	NGC 5845	3.6 μ m	(0.6, 6.02)	ES	3.33	6.02	19.16	3.16	3.27	5.29	19.10	3.18	0.42	0.1213	10.12 \pm 0.26	25.2	8.41 \pm 0.22	SGD19a
79	NGC 6086 ^a	r' (SDSS)	(2.8, 4.65)	E	4.37	13.89	21.68	2.30	4.20	12.41	21.78	2.26	0.46	0.6441	11.52 \pm 0.26	138	9.57 \pm 0.17	SGD19a
80	NGC 6861	3.6 μ m	(0.6, 6.02)	ES	3.07	18.69	19.35	3.08	3.52	20.13	20.17	2.75	0.48	0.1314	10.94 \pm 0.29	27.3	9.30 \pm 0.08	SGD19a
81	NGC 7052 ^a	3.6 μ m	(0.6, 6.02)	E	3.20	34.42	21.84	2.36	3.46	20.04	20.82	2.50	0.46	0.3161	11.46 \pm 0.12	66.4	8.57 \pm 0.23	SGD19a
82	NGC 7332	3.6 μ m	(0.6, 6.02)	EB0	1.78	2.87	16.78	4.11	2.15	2.43	16.92	4.05	0.37	0.1198	10.22 \pm 0.34	24.9	7.11 \pm 0.20	SGD19a
83	NGC 7457	3.6 μ m	(0.6, 6.02)	S0	2.63	6.31	19.62	2.97	2.84	6.51	19.98	2.83	0.42	0.0676	9.40 \pm 0.26	14	7.00 \pm 0.30	SGD19a
84	Circinus	3.6 μ m	(0.45, 6.02)	SABb	2.21	33.26	18.29	3.37	1.80	23.13	18.06	3.47	0.29	0.0204	10.12 \pm 0.2	4.2	6.25 \pm 0.11	DGC19a
85	ESO558-G009 I (HST)	I (HST)	(1.88, 4.52)	Sbc	1.28	0.62	18.17	3.47	1.63	0.68	18.62	3.29	0.31	0.542	9.89 \pm 0.11	115.4	7.26 \pm 0.04	DGC19a
86	IC 2560	3.6 μ m	(0.45, 6.02)	SBb	2.27	7.15	19.64	2.84	0.68	3.92	19.07	3.07	0.15	0.149	9.63 \pm 0.39	31.0	6.49 \pm 0.20	DGC19a
87	J0437+2456 I (HST)	I (HST)	(1.88, 4.52)	SB	1.73	1.22	19.42	2.96	1.97	0.87	19.40	2.97	0.35	0.343	9.90 \pm 0.2	72.8	6.51 \pm 0.05	DGC19a
88	Milky Way	2.4 μ m	...	SBbc	1.32	7.49 ^o	1.32	5.85 ^o	0.38E-4	9.96 \pm 0.05	7.86E-3	6.6 \pm 0.02	GD07
89	Mrk 1029	I (HST)	(1.88, 4.52)	S	1.15	0.47	16.53	4.13	1.07	0.28	16.29	4.23	0.23	0.6392	9.90 \pm 0.11	136.9	6.33 \pm 0.12	DGC19a
90	NGC 0224	3.6 μ m	(0.45, 6.02)	SBb	2.20	418.6	19.58	2.87	1.30	173.6	18.41	3.33	0.22	0.0036	10.11 \pm 0.09	0.8	8.15 \pm 0.16	DGC19a
91	NGC 0253	3.6 μ m	(0.45, 6.02)	SABc	2.53	55.55	19.22	3.00	2.33	27.89	18.82	3.16	0.34	0.0168	9.76 \pm 0.09	3.5	7.00 \pm 0.30	DGC19a
92	NGC 1068	K _s	(0.62, 5.08)	SBb	0.71	10.52	16.17	3.99	0.87	8.29	16.14	4.00	0.20	0.0488	10.27 \pm 0.24	10.1	6.75 \pm 0.08	DGC19a
93	NGC 1097	3.6 μ m	(0.45, 6.02)	SBb	1.95	15.72	18.71	3.21	1.52	11.39	18.27	3.39	0.26	0.1199	10.83 \pm 0.2	24.9	8.38 \pm 0.04	DGC19a
94	NGC 1300	3.6 μ m	(0.45, 6.02)	SBbc	4.20	24.37	21.97	1.91	2.83	7.39	19.99	2.70	0.31	0.07	9.42 \pm 0.25	14.5	7.71 \pm 0.16	DGC19a
95	NGC 1320	3.6 μ m	(0.45, 6.02)	Sa	3.08	3.35	17.93	3.53	2.87	2.23	17.40	3.74	0.38	0.1809	10.25 \pm 0.4	37.7	6.78 \pm 0.29	DGC19a
96	NGC 1398	3.6 μ m	(0.45, 6.02)	SBab	3.44	17.53	19.75	2.80	3.00	10.38	19.04	3.08	0.38	0.1194	10.57 \pm 0.2	24.8	8.03 \pm 0.11	DGC19a
97	NGC 2273 I (HST)	I (HST)	(1.88, 4.52)	SBa	2.24	2.99	18.13	3.47	2.49	3.15	18.52	3.31	0.39	0.1519	9.98 \pm 0.2	31.6	6.97 \pm 0.09	DGC19a
98	NGC 2960	3.6 μ m	(0.45, 6.02)	Sa*	2.59	2.35	18.04	3.49	2.86	2.19	18.30	3.39	0.42	0.338	10.44 \pm 0.36	71.1	7.06 \pm 0.17	DGC19a
99	NGC 2974	3.6 μ m	(0.45, 6.02)	SB	1.56	9.21	18.49	3.30	1.17	6.53	18.12	3.45	0.23	0.1036	10.23 \pm 0.13	21.5	8.23 \pm 0.07	DGC19a
100	NGC 3031 ^b	3.6 μ m	(0.45, 6.02)	Sab	2.81	36.19	18.34	3.35	3.46	42.98	18.93	3.12	0.50	0.0169	10.16 \pm 0.11	3.5	7.83 \pm 0.09	DGC19a
101	NGC 3079	3.6 μ m	(0.45, 6.02)	SBcd	0.52	5.91	16.79	3.98	0.58	4.35	17.13	3.84	0.16	0.0796	9.92 \pm 0.25	16.5	6.38 \pm 0.12	DGC19a
102	NGC 3227	3.6 μ m	(0.45, 6.02)	SABa	2.60	17.91	20.26	2.59	1.90	8.34	19.32	2.97	0.28	0.1017	10.04 \pm 0.17	21.1	7.88 \pm 0.14	DGC19a
103	NGC 3368	3.6 μ m	(0.45, 6.02)	SABa	1.19	5.98	17.07	3.86	1.00	4.83	16.92	3.92	0.21	0.0517	9.81 \pm 0.1	10.7	6.89 \pm 0.09	DGC19a
104	NGC 3393 I (HST)	I (HST)	(1.88, 4.52)	SBa	1.14	1.64	17.27	3.82	1.36	1.77	17.63	3.68	0.27	0.2664	10.23 \pm 0.12	55.8	7.49 \pm 0.05	DGC19a
105	NGC 3627	3.6 μ m	(0.45, 6.02)	SBb	3.17	11.07	18.44	3.32	2.10	3.92	16.98	3.90	0.28	0.0512	9.74 \pm 0.2	10.6	6.95 \pm 0.05	DGC19a
106	NGC 4151	3.6 μ m	(0.45, 6.02)	SABa	2.24	6.23	17.75	3.59	1.85	6.00	17.77	3.59	0.29	0.0916	10.27 \pm 0.15	19.0	7.68 \pm 0.37	DGC19a
107	NGC 4258	3.6 μ m	(0.45, 6.02)	SABb	3.21	41.8	20.14	2.64	2.60	26.4	19.73	3.50	0.34	0.0368	10.05 \pm 0.18	7.6	7.60 \pm 0.01	DGC19a
108	NGC 4303	3.6 μ m	(0.45, 6.02)	SBbc	1.02	2.28	16.51	4.09	0.90	2.16	15.78	4.38	0.20	0.0594	9.42 \pm 0.1	12.3	6.58 \pm 0.17	DGC19a
109	NGC 4388	3.6 μ m	(0.45, 6.02)	SBcd	0.89	21.68	21.68	2.02	1.15	14.3	19.82	2.77	0.24	0.0859	10.07 \pm 0.22	17.8	6.90 \pm 0.11	DGC19a

Table A1 continued

Table A1 (continued)

No.	Galaxy	Band	Υ_λ & $\mathfrak{M}_{\odot,\lambda}$ ($\frac{M_\odot}{L_\odot}$) & mag	Type	n_{maj}	$R_{e,maj}$	$\mu_{e,maj}$	$\log(\frac{I_{e,maj}}{M_\odot/\text{pc}^2})$	n_{eq}	$R_{e,eq}$	$\mu_{e,eq}$	$\log(\frac{I_{e,eq}}{M_\odot/\text{pc}^2})$	C	scale	$\log(\frac{M_{*,sph}}{M_\odot})$	Distance	$\log(\frac{M_{BH}}{M_\odot})$	Ref.
(1)	(2)	(3)	(4)	(5)	(6)	(7)	(8)	(9)	(10)	(11)	(12)	(13)	(14)	(15)	(16)	(17)	(18)	(18)
				arcsec	$\frac{\text{mag}}{\text{arcsec}^2}$	dex	arcsec	$\frac{\text{mag}}{\text{arcsec}^2}$	arcsec	$\frac{\text{mag}}{\text{arcsec}^2}$	dex	dex	$\frac{\text{kpc}}{\text{arcsec}}$	dex	Mpc	dex		
110	NGC 4501	3.6 μm	(0.45, 6.02)	Sb	2.33	21.22	19.53	2.88	2.83	20.35	19.91	2.73	0.44	0.0541	10.11 \pm 0.16	11.2	7.13 \pm 0.08	DGC19a
111	NGC 4594	3.6 μm	(0.45, 6.02)	Sa	6.14	44.94	19.38	2.94	4.24	41.36	19.46	2.91	0.35	0.0462	10.81 \pm 0.2	9.6	8.81 \pm 0.03	DGC19a
112	NGC 4699	3.6 μm	(0.45, 6.02)	SABb	5.35	24.44	19.51	2.89	6.77	29.75	20.31	2.57	0.69	0.1141	11.12 \pm 0.26	23.7	8.34 \pm 0.10	DGC19a
113	NGC 4736 ^b	3.6 μm	(0.45, 6.02)	Sab	0.93	9.79	16.17	4.22	1.03	9.65	16.31	4.17	0.22	0.0214	9.89 \pm 0.09	4.4	6.78 \pm 0.10	DGC19a
114	NGC 4826	3.6 μm	(0.45, 6.02)	Sab	0.73	13.89	17.86	3.55	0.76	11.93	17.98	3.50	0.18	0.0269	9.55 \pm 0.22	5.6	6.07 \pm 0.15	DGC19a
115	NGC 4945 ^b	K _s	(0.62, 5.08)	Sc	3.40	26.33	18.48	3.06	3.19	13.93	17.99	3.26	0.40	0.018	9.39 \pm 0.19	3.7	6.15 \pm 0.30	DGC19a
116	NGC 5055	3.6 μm	(0.45, 6.02)	Sbc	2.02	55.12	20.09	2.66	1.76	43.52	19.85	2.75	0.29	0.0429	10.49 \pm 0.11	8.9	8.94 \pm 0.10	DGC19a
117	NGC 5495	I (HST)	(1.88, 4.52)	SBc	2.60	3.75	20.21	2.65	2.46	3.99	20.23	2.64	0.36	0.4767	10.54 \pm 0.12	101.1	7.04 \pm 0.08	DGC19a
118	NGC 5765b	I (HST)	(1.88, 4.52)	SABb	1.46	1.11	18.72	3.25	1.51	1.00	18.83	3.21	0.28	0.6257	10.04 \pm 0.13	133.9	7.72 \pm 0.05	DGC19a
119	NGC 6264	I (HST)	(1.88, 4.52)	SBb	1.04	1.13	19.23	3.06	1.35	1.05	19.37	3.00	0.27	0.7152	10.01 \pm 0.15	153.9	7.51 \pm 0.06	DGC19a
120	NGC 6323	I (HST)	(1.88, 4.52)	SBab	1.60	1.53	20.39	2.58	1.15	1.71	19.98	2.75	0.22	0.5488	9.86 \pm 0.31	116.9	7.02 \pm 0.14	DGC19a
121	NGC 7582	3.6 μm	(0.45, 6.02)	SBab	2.20	5.33	17.04	3.88	2.21	4.55	17.66	3.63	0.35	0.0959	10.15 \pm 0.2	19.9	7.67 \pm 0.09	DGC19a
122	UGC 3789	I (HST)	(1.88, 4.52)	SABa	2.37	1.60	18.38	3.37	2.67	3.11	19.03	3.11	0.41	0.2372	10.18 \pm 0.14	49.6	7.06 \pm 0.05	DGC19a
123	UGC 6093	I (HST)	(1.88, 4.52)	SBbc	1.55	1.84	19.27	3.04	1.41	1.27	18.87	3.20	0.26	0.7103	10.35 \pm 0.14	152.8	7.41 \pm 0.03	DGC19a

NOTE.—Column: (1) Galaxy name. (2) Wavelength-band (λ) of the image used in parent studies (Column 18). Images for the first 41 galaxies were calibrated to Vega magnitude system and the images of the remaining galaxies (except the Milky Way) were calibrated to AB magnitude system. (3) The stellar mass-to-light ratio (Υ_λ) and the absolute magnitude of the Sun ($\mathfrak{M}_{\odot,\lambda}$) used to obtain the bulge stellar mass. Davis et al. (2019) used a reduced (by 25%) stellar mass-to-light ratio for their LTGs observed at 3.6 μm -band following Querejeta et al. (2015) who reported on the dust glow at 3.6 μm in LTGs. (4) Galaxy morphology based on the multi-component decomposition of the galaxy light performed in studies listed in Column 18. Galaxy mergers are highlighted with an *. (5) Bulge major-axis Sérsic index parameter. (6) Bulge major-axis effective half-light radius. (7) Bulge surface brightness at the corresponding major-axis half-light radius listed in column 6. (8) Logarithm of the bulge intensity at the major-axis half-light radius in the units of M_\odot/pc^2 , calculated using $[(\mu_e - \text{Dist.Mod.} - \mathfrak{M}_{\odot,\lambda} - 2.5 \log(1/\text{scale}^2) - 2.5 \log(\Upsilon_\lambda))/(-2.5)]$ (Graham et al. 2006, their Equation 10). (9)-(12) Similar to columns (5)-(8), but obtained from an independent multi-component decomposition of the galaxy light profile along the equivalent-axis ($R_{\text{eq}} = \sqrt{R_{\text{maj}} * R_{\text{min}}}$). (13) Concentration index (C) calculated using the equivalent-axis bulge Sérsic index and Equation 6 from Trujillo et al. (2001) using $\alpha = 1/3$. (14) Physical scale in kpc arcsec^{-1} , assuming cosmological parameters from Planck Collaboration et al. (2018). (15) Logarithm of the spheroid stellar mass in units of solar mass. (16) Galaxy distance in megaparsec. (17) Logarithm of the directly-measured black hole mass in units of solar mass. (18) Parent studies which performed multi-component decompositions to obtain the bulge parameters. Where SG16=Savorgnan & Graham (2016), SGD19a=Sahu et al. (2019a), DGC19a=Davis et al. (2019), GCS16a=Graham et al. (2016a), GDS16b=Graham et al. (2016b), and GD07=Graham & Driver (2007a). Original sources for black hole mass and distances can be found in Savorgnan et al. (2016), and Sahu et al. (2019a) for ETGs and Davis et al. (2019) for LTGs.

^aGalaxies with a deficit of light at their center, for whom the spheroid profile is parameterized using a core-Sérsic function (Graham et al. 2003b).

^bThe morphology of these spiral galaxies listed on HYPERLEDA (Paturel et al. 2003) or NASA/IPAC Extragalactic Database (NED) suggests a weak bar, however, Davis et al. (2019) did not find evidence of an extended/intermediate bar in these galaxies but rather a nuclear bar.

Table A2. Correlations of $M_{*,\text{sph}}$ and M_{BH} with the bulge equivalent-axis properties ($n_{\text{eq},\text{sph}}$, $C(1/3)$, and $R_{\text{e},\text{sph},\text{eq}}$) calculated using a symmetric application of the MPFITEXY regression (see Section 2)

Category	Number	α	β	ϵ	Δ_{rms}
			dex	dex	dex
(1)	(2)	(3)	(4)	(5)	(6)
$\log(M_{*,\text{sph}}/M_{\odot}) = \alpha \log(n_{\text{sph},\text{eq}}/3) + \beta$					
ETGs	77	3.36 ± 0.20	10.52 ± 0.04	0.30	0.48
LTGs	38	1.47 ± 0.19	10.48 ± 0.06	0.20	0.29
$\log(M_{\text{BH}}/M_{\odot}) = \alpha \log(n_{\text{sph},\text{eq}}/3) + \beta$					
ETGs	77	3.94 ± 0.36	8.18 ± 0.07	0.62	0.73
LTGs	38	2.90 ± 0.55	8.00 ± 0.18	0.63	0.69
$\log(M_{\text{BH}}/M_{\odot}) = \alpha C(1/3)/0.4 + \beta$					
ETGs	77	8.85 ± 0.81	8.10 ± 0.08	0.62	0.72
LTGs	38	7.03 ± 1.50	7.94 ± 0.18	0.64	0.68
$\log(M_{*,\text{sph}}/M_{\odot}) = \alpha \log(R_{\text{e},\text{sph},\text{eq}}) + \beta$					
All Galaxies	115	1.12 ± 0.03	10.42 ± 0.02	0.07	0.25
$\log(M_{\text{BH}}/M_{\odot}) = \alpha \log(R_{\text{e},\text{sph},\text{eq}}) + \beta$					
ETGs with a disk	39	2.08 ± 0.23	8.49 ± 0.09	0.51	0.60
ETGs without a disk	38	2.09 ± 0.35	7.12 ± 0.36	0.53	0.61
ETGs	77	1.30 ± 0.09	8.10 ± 0.06	0.56	0.60
LTGs	38	2.41 ± 0.29	7.79 ± 0.10	0.51	0.60

NOTE—Columns: (1) Subclass of galaxy. (2) Number of galaxies in subclass. (3) Slope of the line obtained from the MPFITEXY(BISECTOR) regression. (4) Intercept of the line obtained from the MPFITEXY(BISECTOR) regression. (5) Intrinsic scatter in the vertical ($\log M_{*,\text{sph}}$ or $\log M_{\text{BH}}$)-direction. (6) Total root mean square (rms) scatter in the vertical direction.